Control of Orienting Movements and Locomotion by Projection-Defined Subsets of Brainstem V2a Neurons

Giovanni Usseglio, Edwin Gatier, Aurélie Heuzé, Coralie Hérent, Julien Bouvier

Article

Current Biology

Control of Orienting Movements and Locomotion by Projection-Defined Subsets of Brainstem V2a Neurons

Graphical Abstract

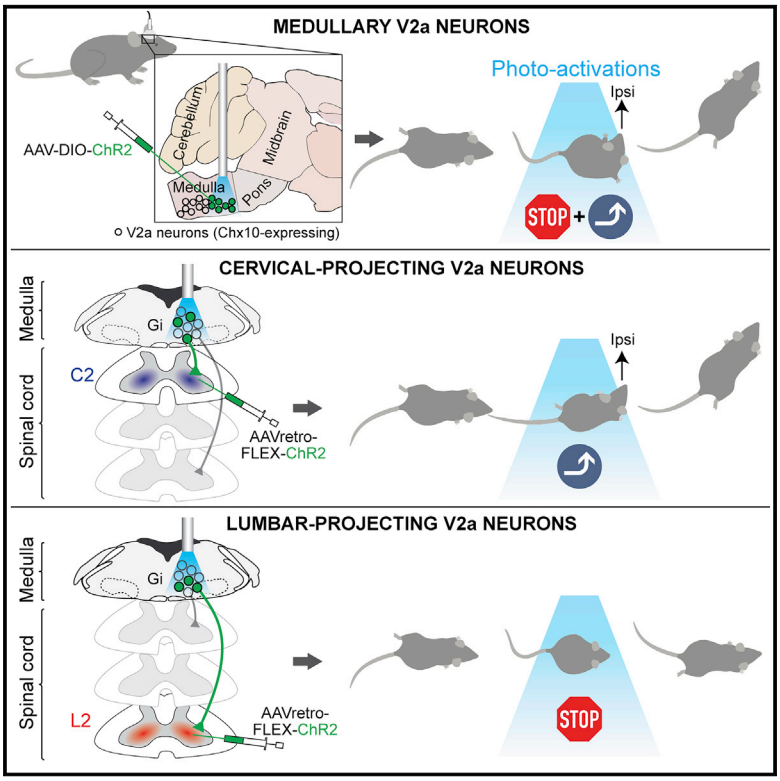

Highlights

- Brainstem V2a neurons control orienting movements, locomotor speed, and trajectory
- Distinct V2a subsets contact the cervical and lumbar spinal segments
- Cervical-projecting V2a neurons govern the head orientation and the path trajectory
- Lumbar-projecting V2a neurons are dedicated to control locomotor velocity

Authors

Giovanni Usseglio, Edwin Gatier, Aurélie Heuzé, Coralie Hérent, Julien Bouvier

Correspondence

julien.bouvier@cnrs.fr

In Brief

Usseglio et al. demonstrate that V2a neurons, a genetically circumscribed class of excitatory reticular neurons, control multiple motor actions linked to orientation. Using viral tracings and circuit optogenetics, they further uncover a modular organization of this neuronal class, with projection-defined subtypes that each support one motor action.

Usseglio et al., 2020, Current Biology *30*, 1–17
December 7, 2020
https://doi.org/10.1016/j.cub.2020.09.014

CellPress

Current Biology

CellPress
OPEN ACCESS

Article

Control of Orienting Movements and Locomotion by Projection-Defined Subsets of Brainstem V2a Neurons

Giovanni Usseglio,[1] Edwin Gatier,[1] Aurélie Heuzé,[1] Coralie Hérent,[1] and Julien Bouvier[1,2,*]
[1]Université Paris-Saclay, CNRS, Institut des Neurosciences Paris-Saclay, 91190 Gif-Sur-Yvette, France
[2]Lead Contact
*Correspondence: julien.bouvier@cnrs.fr
https://doi.org/10.1016/j.cub.2020.09.014

SUMMARY

Spatial orientation requires the execution of lateralized movements and a change in the animal's heading in response to multiple sensory modalities. While much research has focused on the circuits for sensory integration, chiefly to the midbrain superior colliculus (SC), the downstream cells and circuits that engage adequate motor actions have remained elusive. Furthermore, the mechanisms supporting trajectory changes are still speculative. Here, using transneuronal viral tracings in mice, we show that brainstem V2a neurons, a genetically defined subtype of glutamatergic neurons of the reticular formation, receive putative synaptic inputs from the contralateral SC. This makes them a candidate relay of lateralized orienting commands. We next show that unilateral optogenetic activations of brainstem V2a neurons *in vivo* evoked ipsilateral orienting-like responses of the head and the nose tip on stationary mice. When animals are walking, similar stimulations impose a transient locomotor arrest followed by a change of trajectory. Third, we reveal that these distinct motor actions are controlled by dedicated V2a subsets each projecting to a specific spinal cord segment, with at least (1) a lumbar-projecting subset whose unilateral activation specifically controls locomotor speed but neither impacts trajectory nor evokes orienting movements, and (2) a cervical-projecting subset dedicated to head orientation, but not to locomotor speed. Activating the latter subset suffices to steer the animals' directional heading, placing the head orientation as the prime driver of locomotor trajectory. V2a neurons and their modular organization may therefore underlie the orchestration of multiple motor actions during multi-faceted orienting behaviors.

INTRODUCTION

Our capacity to continuously adjust our attention and directional heading in response to internal goals or external stimuli is vital. It supports a large panel of behaviors including spatial navigation, exploration of the environment, feeding, and defense. In order to achieve this, animals mobilize lateralized motor actions that are often tightly coupled. In the animal's reference frame, coordinated movements of the head, the eyes, and in rodents, the orofacial sensors represent the primary mean to displace the visual axis and the sensory apparatus toward a point in space [1–3]. When the animal is on the move, these "strict" orienting responses are accompanied by a change in limb activity to reduce locomotor speed, to allow fixation and exploration of a fixed cue, and/or when needed, to change the path trajectory. How the brain orchestrates these multiple motor actions is still only partly resolved. Additionally, the mechanical substrate for trajectory changes during ongoing locomotion, whether it is head orientation [4–6], an asymmetric descending drive to limb controllers [7, 8], or a combination of both, has remained speculative. Much attention has been given to circuits for sensory integration, mainly to the superior colliculus (SC; reviewed in [9]). This midbrain structure synthesizes inputs from different sensory modalities and controls spatially targeted motion in the large sense, including head-eye responses, orofacial movements, and locomotor trajectory [10–14]. However, the cells and circuits that are downstream of the SC and relay orienting commands to the adequate motor groups have remained elusive.

The reticular formation (RF) of the pons and medulla is well known to control movements and is a candidate relay of orienting commands. First, the output layers of the SC project abundantly to the RF [15, 16]. Second, it hosts the circuits for ocular and orofacial movements [17, 18] as well as reticulospinal (RS) neurons that directly reach the spinal cord [19]. In particular, neck motoneurons of the upper cervical spinal cord that control the head orientation are contacted by RS neurons of the gigantocellular (Gi) reticular nucleus [20–22]. The timing and velocity of hindlimb movements, controlled by the lumbar spinal cord [23, 24], are also critically dependent on descending signals from the Gi and adjacent nuclei [25–28]. Third, left-right unbalanced activation or inhibition of the RF has been linked to head orienting movements [26, 29] and to the steering of swimming in the lamprey [8] and of locomotor-like activities on neonatal rat *in vitro* preparations [7]. However, these investigations did not determine the identity of reticular neurons that are downstream of the SC and mediate orienting responses, or examine their

Please cite this article in press as: Usseglio et al., Control of Orienting Movements and Locomotion by Projection-Defined Subsets of Brainstem V2a Neurons, Current Biology (2020), https://doi.org/10.1016/j.cub.2020.09.014

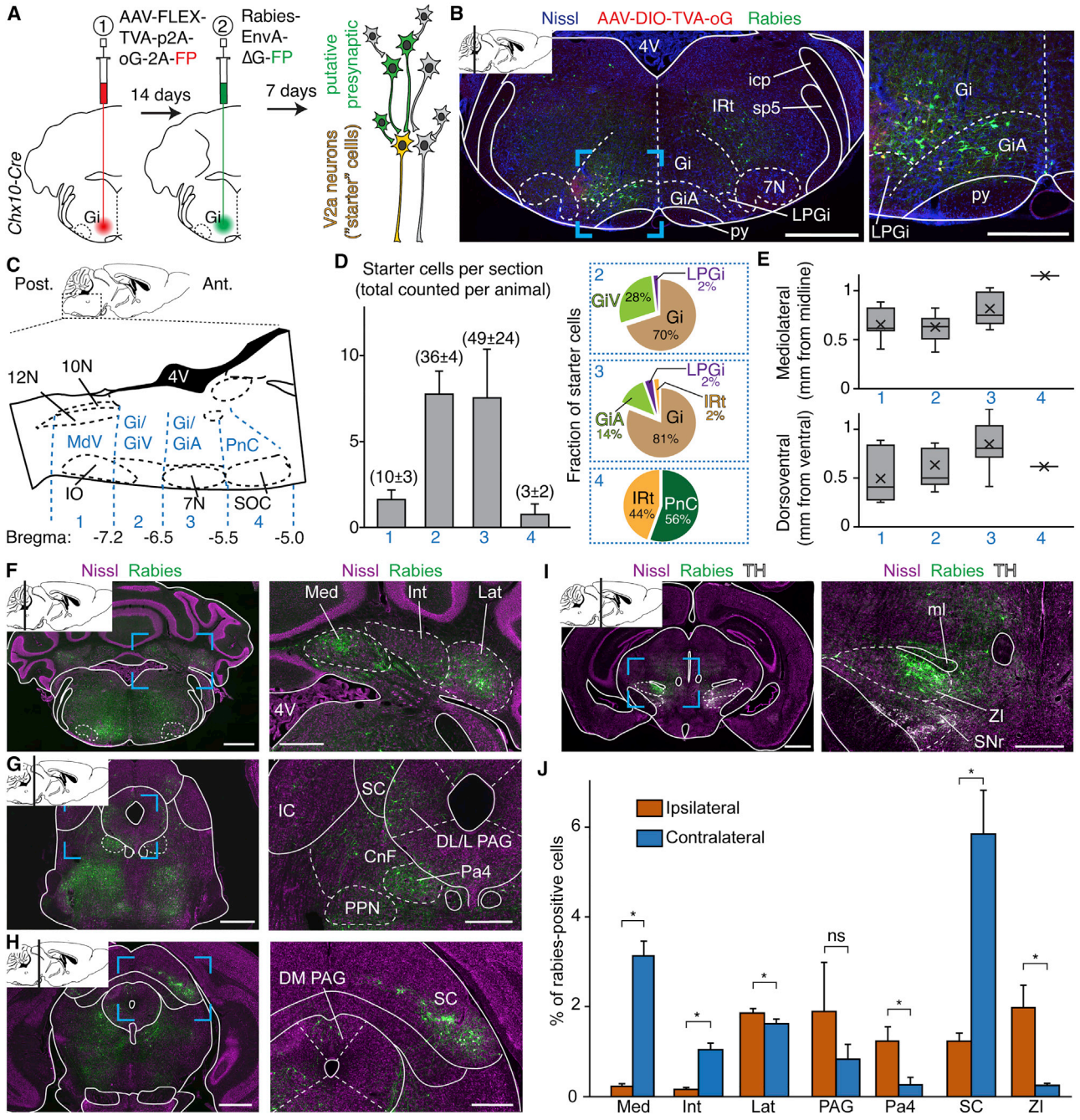

Figure 1. Retrograde Transneuronal Viral Strategy Reveals the Upstream Circuits of V2a Gi Neurons

(A) Schematics of the injection of the helper virus coding TVA and oG (1) and the EnvA-ΔG-rabies (Rb) virus (2) unilaterally in the left Gi of a *Chx10-Cre* adult mouse.

(B) Transverse brainstem section at the level of the injection site showing V2a neurons transfected with the helper virus (red), those co-transfected with the Rb virus ("starter" cells, yellow), and their putative presynaptic partners (Rb only, green), on a Nissl background (blue). Scale bar, 1 mm. Inset to the right is an enlargement of the blue boxed area. Scale bar, 500 μm.

(C) Sagittal schematic of the brainstem indicating the rostrocaudal levels (1 to 4) used for reporting starter cells.

(D) Bar graph showing the average number ± SEM of starter cells per histological section, and in brackets the average total ± SEM per animal, at the 4 rostrocaudal levels (total starter cells counted: 299 from 3 animals; average per animal: 100 ± 29). Pie graphs to the right show the distribution, within rostrocaudal levels 2, 3, and 4, of starter neurons in the indicated subnuclei (in percent of all starter cells at each level, pooled from the 3 animals). All cells at the rostrocaudal level 1 were in the MdV. See STAR Methods for the delineation of brainstem nuclei.

(E) Mediolateral (top, in mm from the midline) and dorsoventral (bottom, in mm from the ventral border) positions of starter cells at each rostrocaudal level (pooled from 299 cells from 3 animals) presented as the mean (crosses) and box-and-whisker plots, which give the median, 25th and 75th percentiles, and range.

(F–I) Transverse sections showing Rb^{+} cells (green) at various rostrocaudal locations on a Nissl background (magenta). A tyrosine hydroxylase staining (TH, gray) is added in (I) to identify the SNr. Scale bars, 1 mm and 500 μm (insets).

(legend continued on next page)

Please cite this article in press as: Usseglio et al., Control of Orienting Movements and Locomotion by Projection-Defined Subsets of Brainstem V2a Neurons, Current Biology (2020), https://doi.org/10.1016/j.cub.2020.09.014

implication to trajectory changes during limbed locomotion *in vivo*. Another significant gap of knowledge concerns the possibility for a synergistic control of distinct motor actions by a unique population, or by instead distinct subsets, of reticular neurons. Specifically, movements of the head, orofacial sensors, and locomotor velocity and direction are often tightly coupled [1, 2, 4, 5], and the existence of reticular neurons with branched axonal collaterals [19, 21] raises the possibility for a common control by a unique neuronal population. Yet this remained to be supported experimentally.

Here we investigated the possibility that brainstem V2a neurons, a genetically circumscribed neuronal class defined by the expression of the transcription factor Chx10 [30, 31], may control orienting motor actions. Indeed, they represent a subgroup of excitatory glutamatergic neurons located in the ventral RF, including in the Gi nucleus [32, 33]. Photo-activation of V2a Gi neurons in mice unexpectedly depresses spinal locomotor circuits [34], and this function could participate in steering locomotor trajectory [35]. Second, V2a neurons collectivity send both local and spinal projections [32–36], raising the possibility that this population, or subsets thereof, may drive other motor actions in synergy with limb control. However, these neurons have globally not been incorporated into the framework for studying orientation and nothing is known about their putative diversity.

Using transneuronal viral tracings, we show that V2a Gi neurons receive putative inputs from the contralateral SC, making them candidates for relaying lateralized orienting commands. Next, we found that unilateral photo-activations of V2a Gi neurons both evoked orienting-like motor responses on still animals and can halt and steer the locomotor trajectory when animals are on the move. Finally, and this is a major finding reported here, we reveal distinct functional subsets of V2a RS neurons with at least (1) a lumbar-projecting subset that controls locomotor velocity, but does not impact trajectory even when activated unilaterally, and (2) a cervical-projecting subset dedicated to head orientation and whose activation suffices to steer locomotor trajectory. These findings establish that multiple motor components of orientation are controlled by distinct reticular neurons that share a common genetic identity but that differ in their efferent connectivity. Furthermore, our work argues that the head orientation acts as the prime driver for steering locomotor trajectory.

RESULTS

V2a Gi Neurons Receive Putative Inputs from the Contralateral Superior Colliculus

To address whether V2a Gi neurons are embedded in circuits for orientation, we used a genetically restricted two-virus approach [37] to anatomically reveal their putative inputs (Figure 1A). Specifically, a cre-dependent AAV helper vector (AAV-DIO-TVA-oG-GFP; STAR Methods) was injected unilaterally in the Gi of *Chx10-Cre* adult mice [34, 38, 39], followed by a G-deleted and EnvA-pseudotyped rabies (Rb) virus coding mCherry. We aimed at transfecting V2a neurons unilaterally and located within the intermediate and rostral medullary reticular formation, i.e., rostrocaudal levels that house the Gi and its ventral and alpha parts (GiA/GiV; Figures 1B–1D) where V2a neurons that arrest locomotion are located [34]. Occasional starter cells were found in the adjacent intermediate reticular nucleus (IRt) and the lateral paragigantocellular nucleus (LPGi; Figure 1D), also known to contain V2a neurons [36]. Transneuronally labeled neurons, i.e., expressing only the Rb-driven fluorophore, were detected throughout the brainstem and to a lower extent in the diencephalon. A large proportion of Rb-positive cells was found in the medullary and pontine reticular formations, both ipsilaterally (15% ± 2% of total Rb^+ cells) and contralaterally (15% ± 3%). Aside from this local connectivity, labeling was detected in the deep cerebellar nuclei with various degrees of lateralization (Figures 1F and 1J). In the midbrain, confined labeling was seen in the periaqueductal gray and the mesencephalic reticular formation, notably in what may correspond to the paratrochlear nucleus (Pa4; Figures 1G and 1J). We found no Rb^+ cells in the cuneiform and pedunculopontine nuclei (CnF and PPN; Figure 1G), forming the mesencephalic locomotor region that controls forward locomotion [40, 41]. Importantly, the highest proportion of transneuronally labeled neurons aside from the reticular formation was observed in the SC, predominantly contralaterally (Figures 1H and 1J). Confined labeling was also observed in the zona incerta, mostly ipsilaterally (Figures 1I and 1J). More rostrally, only sparse Rb^+ cells were seen in the somatosensory and motor cortices (data not shown). These experiments indicate that V2a neurons of the Gi and adjacent nuclei are downstream of the SC and may therefore relay lateralized orienting commands.

Activating V2a Gi Neurons Unilaterally Evokes Orienting Motor Responses

To evaluate the capacity of V2a Gi neurons to mediate orienting movements when activated unilaterally, we virally delivered the Channelrhodopsin 2 (ChR2) in the Gi on one side (AAV-DIO-ChR2-eYFP) of *Chx10-Cre* mice and implanted an optic fiber on the same side (Figures 2A and 2B). We confined transfections sites unilaterally and to the rostral medulla, i.e., encompassing the Gi and the adjacent GiA nuclei (Figure S1A), where the strongest inhibitory effect on locomotion was reported [34]. We did not attempt to target smaller contingents (e.g., GiA versus Gi); we will therefore refer to V2a Gi neurons throughout the study.

When light stimulations were delivered unilaterally (500 ms trains of 15 ms pulses at 40 Hz) on stationary mice, the most

(J) Mean percentage ± SEM of Rb^+ cells in a given region over the total amount of Rb^+ cells (n = 3 animals, total cells counted: 8,157; average per animal: 2,719 ± 139). Regions presented are those showing the highest proportions of Rb^+ cells, outside of the RF, which accounted for 15% ± 2% ipsilaterally and 15% ± 3% contralaterally.

4V, fourth ventricle; sp5, spinal trigeminal tract; Gi, gigantocellular reticular nucleus; GiA, gigantocellular reticular nucleus alpha part; GiV, gigantocellular reticular nucleus ventral part; LPGi, lateral paragigantocellular nucleus; IRt, intermediate reticular nucleus; 7N, facial nucleus; py, pyramidal tract; Med, medial (fastigial) nucleus; Int, interposed nucleus; Lat, lateral (dentate) nucleus; IC, inferior colliculus; SC, superior colliculus; LPAG, lateral periaqueductal gray; DLPAG, dorsolateral periaqueductal gray; DMPAG, dorsomedial periaqueductal gray; CnF, cuneiform nucleus; PPN, pedunculopontine nucleus; Pa4, parathroclear nucleus; ml, medial lemniscus; Zl, zona incerta; SNr, substantia nigra pars reticulata.

Please cite this article in press as: Usseglio et al., Control of Orienting Movements and Locomotion by Projection-Defined Subsets of Brainstem V2a Neurons, Current Biology (2020), https://doi.org/10.1016/j.cub.2020.09.014

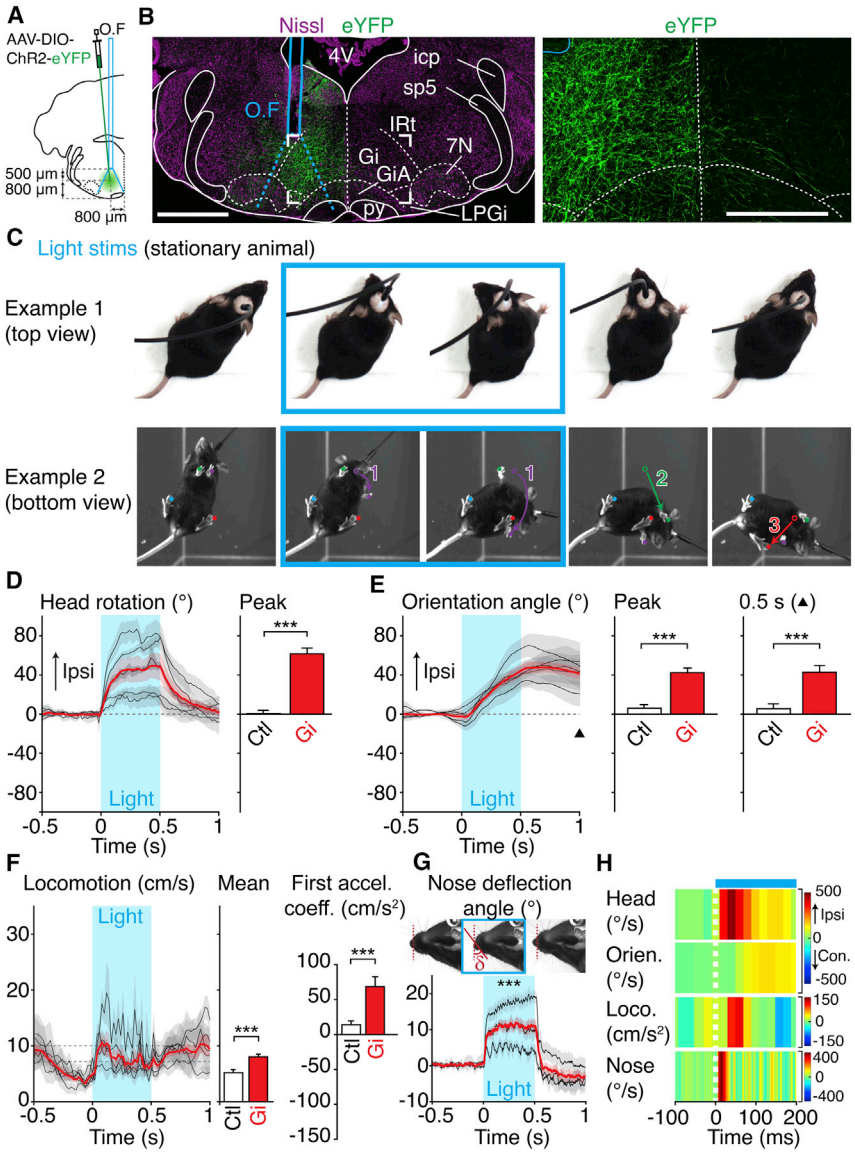

Figure 2. Unilateral Photo-Activations of V2a Gi Neurons Evoke Orienting-like Motor Responses

(A) Experimental strategy for photo-activating V2a Gi neurons. OF, optic fiber. The injection pipette is depicted with an angle for clarity, but the injection was performed without angle.

(B) Left: transverse section at the level of the Gi showing transfected V2a neurons (eYFP, green) on a Nissl background (magenta), the position of the OF, and the theoretical light cone at the fiber tip (dashed blue lines). Scale bar, 1 mm. Right: close-up view over the boxed area showing that transfected neurons are strictly restricted to the ipsilateral side. The vertical dashed line depicts the midline. Scale bar, 500 µm. See also Figure S1A.

(C) Two example snapshots from two animals, showing the typical head yaw rotation and the possible change in orientation evoked by the photo-activation of V2a Gi neurons (15 ms pulses at 40 Hz, for a duration of 500 ms, in blue). On the bottom view, colored numbers indicate the order of limb movements. See also Video S1.

(D–F) Left: mean ± SEM light-evoked changes in head yaw rotation (D), body orientation (E), and locomotor speed (F) for each animal (gray, n = 5 animals, 7 trials each) and across animals (red). The black arrowhead in (E) indicates the time point at 0.5 s after light offset. The dashed zone in (F) indicates the threshold from stationary (<7.5 cm/s) to locomoting (>10 cm/s) conditions. Bar graphs to the right show the mean ± SEM of the peak head rotation during photo-activations (D), the peak change in orientation during photo-activations and the orientation angle 0.5 s after light offset (E), and the mean locomotor speed and the first acceleration coefficient during photo-activations (F) across all trials (Gi, n = 35 trials from 5 mice, 7 trials each) compared with mock trials from control mice (Ctl, n = 44 trials from 4 mice, 11 trials each). ***p < 0.001 (unpaired t test). See also Figure S2 for the calculation of movements and the responses of control mice.

(G) Top: snapshots of one head-fixed animal showing the angular displacement of the snout (δ). Bottom: mean angular deflection ± SEM of the snout normalized to the angle during the same time interval before light onset, for each animal (gray) and across animals (red). ***p < 0.001 (paired t test between mean values 0.5 s before and during the 0.5 s photo-activations, n = 15 trials from 3 mice, 5 trials each).

(H) Color plot showing the first derivative of the above motor parameters from 100 ms before to 200 ms after light onset (the dashed white line indicates light onset). Note the rapid occurrence of nose deflection (peak change at 15 ms), followed by the head rotation (peak change at 40 ms) and the delayed change in body orientation (peak at 140 ms).

striking response was a robust rotation of the head in the yaw axis and a displacement of the body orientation toward the stimulated side (Figures 2C–2E; Video S1; see STAR Methods and Figures S2A–S2D for movement calculations). These movements were not seen in mock trials on injected and implanted wild-type mice (Figures S2E–S2H), which served as the reference for statistical comparisons in freely moving situations throughout this study (bar graphs in Figures 2D–2F). Photo-activations did not engage animals in sustained locomotor activity, but the forelimbs could perform one or two steps to maintain the body orientation with that of the head (Figures 2C and 2F). Following light offset, animals could regain their initial orientation, but in the majority of trials, they remained oriented toward the stimulated side (Figure 2E; compare also examples in Figure 2C and Video S1). Examinations on head-fixed animals revealed that photo-activations also evoked an immediate horizontal deflection of the snout tip toward the stimulated side (Figure 2G), known to accompany head orienting movements [2]. Finally, to examine the relative temporal occurrences of these motor responses, we computed and color-plotted the first derivative of each parameter after light onset (Figure 2H). This revealed that the change in nose positioning peaked first, on average at 15 ms after light onset, rapidly followed by the head rotation (at 40 ms), suggesting that these are the primary

Please cite this article in press as: Usseglio et al., Control of Orienting Movements and Locomotion by Projection-Defined Subsets of Brainstem V2a Neurons, Current Biology (2020), https://doi.org/10.1016/j.cub.2020.09.014

CellPress
OPEN ACCESS

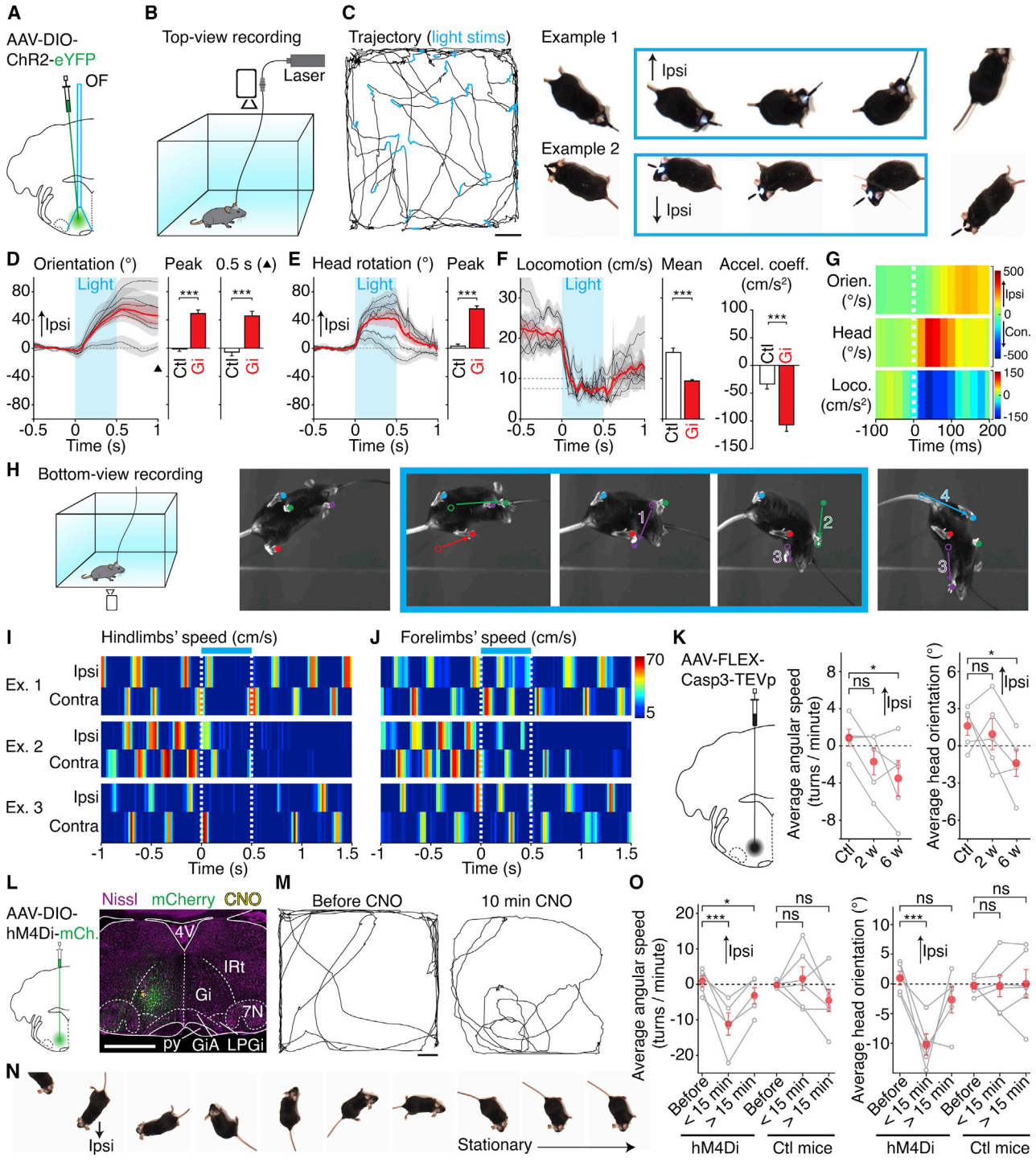

Figure 3. V2a Gi Neurons Control Locomotor Trajectory

(A) Experimental strategy for photo-activating V2a Gi neurons. OF, optic fiber. The injection pipette is depicted with an angle for clarity, but the injection was performed without angle. See also Figure S1A.

(B) Setup for top-view video recordings in an open field.

(C) Left: trajectory of one representative mouse for 3 min showing abrupt photo-evoked directional changes (15 ms pulses at 40 Hz, for a duration of 500 ms, in blue). Scale bar, 10 cm. Right: two example snapshots from two mice showing the typical light-evoked change of locomotor trajectory. See also Video S2.

(D–F) Left: mean ± SEM light-evoked changes in body orientation (D), head yaw rotation (E), and locomotor speed (F) of each animal (gray, n = 6 mice, 8 trials each) and across animals (red). The black arrowhead in (D) indicates the time point at 0.5 s after light offset. The dashed zone in (F) indicates the threshold from stationary (<7.5 cm/s) to locomoting (>10 cm/s) conditions. Bar graphs to the right show the mean ± SEM of the peak change in orientation during photo-activations and the orientation angle 0.5 s after light offset (D), the peak head rotation (E), and the mean locomotor speed and the first acceleration coefficient during

(legend continued on next page)

Please cite this article in press as: Usseglio et al., Control of Orienting Movements and Locomotion by Projection-Defined Subsets of Brainstem V2a Neurons, Current Biology (2020), https://doi.org/10.1016/j.cub.2020.09.014

responses evoked. The change of body orientation occurred later with a peak angular speed at 140 ms. Altogether, these results indicate that activating V2a neurons in the Gi unilaterally evokes known motor components of oriented attention in rodents [2, 14, 42].

Activating V2a Gi Neurons Unilaterally during Locomotion Changes Trajectory

The orienting-like responses described above prompted us to test whether V2a Gi neurons also impact locomotor trajectory when animals are moving. For this, injected and implanted animals were placed in an open field and tracked from above (Figures 3A and 3B) while pulsed light stimulations were delivered during locomotion (i.e., instantaneous speed > 10 cm/s). We observed a striking and pronounced change of locomotor trajectory toward the stimulated side that persisted after light offset (Figures 3C and 3D; Video S2). This orientation change is associated with a rotation of the head (Figures 3C and 3E), reminiscent of the still trials. Additionally, locomotor speed was strongly reduced and animals reached the stationary threshold within 130 ± 30 ms of light onset (Figures 3C and 3F). This progressive locomotor halt, obtained here from strict unilateral activations (Figure S1A), recalls what was reported previously when activating the same cells bilaterally [34]. These motor changes were, however, not seen in, and are thus significantly different from, mock trials in control mice (bar graphs in Figures 3D–3F; see Figures S2I–S2K for responses of control mice). Temporal examination of the evoked motor sequence revealed that the head rotation and the locomotor deceleration occurred first and concomitantly (both peaked at 40 ms), followed by the body orientation (peak at 140 ms; Figure 3G). Manual tracking of the animal's paws showed that, during photo-activations, the hindlimbs terminate the ongoing step before remaining immobile and positioned symmetrically while the forelimbs performed left-right alternating movements toward the stimulated side (Figures 3H–3J; Video S2). When the animals resumed walking after light offset, they did so in the direction pointed by the head. Activating V2a Gi neurons unilaterally during ongoing locomotion therefore imposes a rapid yaw rotation of the head, a bilateral arrest of the hindlimbs, and a displacement of the forelimbs, altogether leading to a change of trajectory. Interestingly, these motor actions can also be expressed during naturally occurring changes in direction. Specifically, however, while the head yaw rotation often precedes the change in body orientation, the relative timing, or even the presence at all, of a locomotor deceleration was more variable (Figures S3A and S3B). Indeed, we found examples of turnings associated with a transient arrest of the 4 limbs followed by a reprise driven by the forelimbs, as well as some with continuing alternating movements of the 4 limbs (Figure S3C). This suggests that the motor sequence evoked by the photo-activation of V2a neurons can be mobilized, in whole or in part, during spontaneous directional changes.

Ablating V2a Gi Neurons or Impairing Their Activity Unilaterally Biases Locomotor Trajectory

We next addressed whether V2a Gi neurons are required for spontaneous changes of locomotor trajectory. We first virally delivered the genetically engineered caspase-3 unilaterally to V2a Gi neurons, to commit them to apoptosis [43]. In an open field test, injected animals showed a time-dependent bias to turn on the contralateral side (Figure 3K). Since this approach may mobilize compensatory circuits and does not allow us to quantify cell death, we next transiently silenced V2a Gi neurons using the inhibitory DREADD hM4Di delivered virally. Four weeks later, intracranial delivery of 1 m CNO was performed by another surgery (Figure 3L). Injections were unilaterally restricted and comparable to those of optogenetic activations, i.e., targeted to the Gi and GiA of the rostral medulla (Figure S1B). When examined immediately after the CNO delivery, animals showed only few episodes of locomotion owing to the partial recovery from anesthesia. Yet when they engaged in walking, either spontaneously or following motivation by the experimenter, they showed a very strong bias toward the contralateral side (Figures 3M–3O; Video S3). Moreover, the head was abnormally bent

photo-activations (F) across all trials (Gi) compared with mock trials from control mice (Ctl, n = 48 trials from 4 mice, 12 trials each). ***p < 0.001 (unpaired t test). See also Figure S2 for the calculation of movement changes and responses of control mice.

(G) Color plot of the first derivative of each motor parameter showing their temporal evolution from 100 ms before to 200 ms after light onset (the dashed white line indicates light onset). Note the rapid head movement and locomotor deceleration and the delayed change in body orientation.

(H) Setup for bottom-view video recordings and one example of a photo-evoked trajectory change. Colored numbers indicate the order of limb movements. See also Video S2 for the corresponding video and another example and Figure S3 for naturally occurring turns.

(I and J) Color plots of the velocity of the paws of the hindlimbs (I) and forelimbs (J) from 1 s before to 1 s after the 500 ms photo-activation. The y axis represents 3 example trials from distinct animals; the top one is shown in (H). The color gradient to red indicates speed values in cm/s. During photo-activations, the hindlimbs remain still after having terminated the ongoing step but the forelimbs continue moving.

(K) Caspase3-mediated ablation of V2a Gi neurons leads to a time-dependent increase of spontaneous turns toward the contralateral side, represented as the average angular speed per minute of walking (i.e., instantaneous speed > 10 cm/s), and to a biased orientation of the head. Gray open circles are the means of individual animals, and red circles are the means ± SEM across animals. 2 w, 2 weeks post-injection; 6 w, 6 weeks post-injection. Number of videos: Ctl, 13; 2w, 10; 6w, 11 (from 5 mice). *p < 0.05; ns, not significant (unpaired t test).

(L) Transient silencing of V2a Gi neurons by an hM4Di virus followed by intracranial delivery of 1 mM CNO by surgery (detected by fluorescent beads, yellow). Scale bar, 1 mm. See also Figures S1B and S1C.

(M) Trajectory of one representative mouse during 3 min in an open field before and 10 min after intracranial CNO delivery. Scale bar, 10 cm.

(N) Snapshots, taken every 500 ms, of one representative animal injected on the left side, showing a bias in locomotor trajectory and head position, even during stationary periods, toward the contralateral side. See also Video S3.

(O) Average angular speed per minute of walking (left) and average head rotation angle (right) showing the significant bias toward the contralateral side of hM4Di-injected CNO-treated mice (hM4Di, number of videos: before, 13; <15 min, 10; >15 min, 11; from 5 mice), but not following CNO delivery alone using a similar surgical procedure (Ctl mice, number of videos: before, 17; <15 min, 10; >15 min, 12; from 5 mice). Gray open circles are the means of individual animals, and red circles are the means ± SEM across animals. *p < 0.05; ***p < 0.001; ns, not significant (unpaired t test).

Please cite this article in press as: Usseglio et al., Control of Orienting Movements and Locomotion by Projection-Defined Subsets of Brainstem V2a Neurons, Current Biology (2020), https://doi.org/10.1016/j.cub.2020.09.014

CellPress
OPEN ACCESS

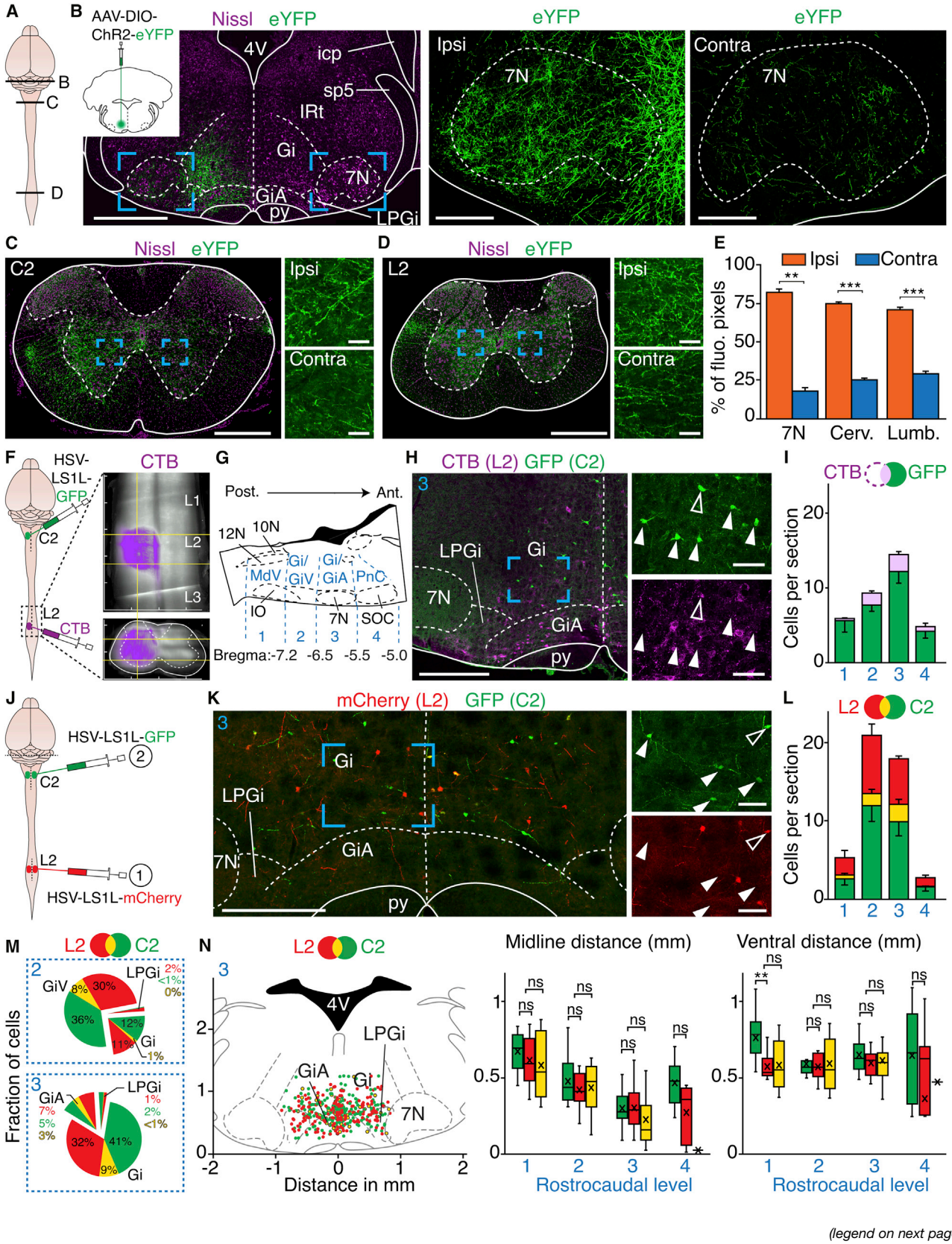

(legend on next page)

Please cite this article in press as: Usseglio et al., Control of Orienting Movements and Locomotion by Projection-Defined Subsets of Brainstem V2a Neurons, Current Biology (2020), https://doi.org/10.1016/j.cub.2020.09.014

toward the contralateral side, an effect also noticeable during stationary periods (Figures 3N and 3O; Video S3). To exclude that these motor abnormalities are caused by the surgical procedure used to deliver the CNO, control (wild-type) mice that did not receive the hM4Di virus underwent a similar procedure, including anesthesia, CNO injection, and behavioral testing. These showed globally no bias toward the ipsilateral or contralateral sides (Figure 3O). The activity of V2a Gi neurons is therefore necessary for controlling locomotor trajectory and may also help to maintain an upright head position.

Distinct Subsets of V2a RS Neurons Show Preferential Projections to Specific Spinal Segments

Since V2a Gi neurons control multiple oriented actions, they should have lateralized access to the corresponding motor circuits. Indeed, V2a axonal projections densely innervate the facial motor nucleus (7N), associated with the whisker and snout musculature [17], as well as the upper cervical and lumbar segments, containing, respectively, the neck [20] and hindlimb [23, 24] motor circuits (Figures 4A–4D). Projections were found on both sides with a predominant ipsilateral contribution (Figure 4E). We next addressed whether these distinct target regions are contacted by a unique population of V2a neurons with branched collaterals or, instead, by distinct subsets with target-specific projections. For the rest of the study, we focused on the head rotation, body orientation, and control of the hindlimbs since these actions are piloted by spinal circuits and may therefore be under a common control by branched RS neurons. We first combined a Cre-dependent retrogradely transported herpes-simplex virus (HSV) [44, 45], injected into the 2nd cervical segment (C2), with cholera toxin B (CTB) injected into the 2nd lumbar segment (L2; Figure 4F). Retrogradely labeled V2a neurons from C2 were found throughout the RF, but only a minority were co-labeled with CTB (14% ± 2% overall; 12% ± 3% at the level of the Gi/GiA where optogenetic activations are performed; Figures 4G–4I). This indicates that the majority of V2a neurons do not have access to both spinal levels. To corroborate this further, we retrogradely labeled V2a neurons from both the C2 and L2 segments conjointly, using two Cre-dependent HSVs each coding a distinct fluorophore (Figure 4J). The majority of labeled V2a neurons were again expressing one, but rarely both, fluorophores (Figures 4K and 4L). Specifically, at rostrocaudal levels where photo-activations are performed, double-labeled V2a neurons represented only 11% ± 2% of all labeled cells. In contrast, when the two HSVs were injected at the same spinal segment (L2) either conjointly or sequentially, we found >90% of co-labeling (Figure S4), confirming previous reports that multiple HSVs can be expressed in individual cells [46]. Therefore, the preferential expression of either fluorophore in the dual C2/L2 HSV injection reflects the existence of distinct V2a subsets each having preferential projections to a specific spinal segment. Interestingly, these subsets were similarly distributed across the different nuclei of the ventral RF (Figures 4L and 4M). Moreover, reporting their mediolateral and dorsoventral positioning did not reveal any spatial segregation except at caudal-most levels (MdV) where the C2-projecting ones tended to be positioned more dorsally (Figure 4N). Finally, using a projection-based delivery of the rabies proteins oG and TVA, we found that both the C2 and L2-projecting V2a subsets receive inputs from the SC and, qualitatively, share similar input structures, albeit in varied proportions and with lower degrees of lateralization than the overall population (Figure S5). These observations altogether demonstrate the existence of distinct

Figure 4. Distinct but Spatially Intermingled V2a RS Neurons Show Preferential Projections to Specific Spinal Segments

(A) Schematic illustrating the position of the sections displayed in the following panels.

(B) Left: transverse section at the level of the Gi, where optogenetic activations are performed, showing the unilateral transfection of V2a neurons with an AAV-DIO-ChR2-eYFP. Scale bar, 1 mm. Right: magnifications of the blue boxed areas showing V2a projections in the ipsilateral and contralateral facial motor nuclei (7N). Scale bar, 200 μm.

(C and D) Transverse spinal cord sections from the same animal (representative of 3 mice), showing V2a projections at the 2nd cervical (C2) and 2nd lumbar (L2) levels. Dashed lines delineate the white matter. Scale bars, 500 μm and 50 μm (insets).

(E) Bar graphs showing the average percentage ± SEM of eYFP^{+} pixels located ipsilaterally and contralaterally in the 7N and in the cervical and lumbar white matter. ***$p < 0.001$; **$p < 0.01$ (unpaired t test; 7N, 10 sections; spinal cord, 12 sections; from n = 3 mice).

(F) Left: experimental strategy for labeling V2a RS neurons projecting to C2 with a Cre-dependent HSV and all L2-projecting neurons with CTB. LS1L, Lox-Stop-Lox. Right: example blend projection along the rostrocaudal (top) and transverse axis (bottom) of a CUBIC-cleared spinal cord imaged with light-sheet microscopy, showing the typical spread of dye load following an injection of CTB at L2 unilaterally. Thick marks, 500 μm.

(G) Sagittal schematic of the brainstem indicating the rostrocaudal levels (1 to 4, in blue), used for reporting labeled neurons.

(H) Transverse section (representative of 4 mice) at the rostrocaudal level 3 showing C2-projecting V2a neurons (GFP) and all lumbar-projecting neurons (CTB). Scale bar, 500 μm. Insets to the right are magnifications of the blue boxed area, showing the scarcity of double-labeled neurons (open arrowheads). Scale bar, 100 μm.

(I) Bar graphs showing, at the 4 rostrocaudal levels, the average number ± SEM of HSV and HSV;CTB-labeled neurons per histological section (n = 4 mice, 756 HSV^{+} cells counted in total; average per animal, 189 ± 24).

(J) Viral strategy for labeling V2a RS neurons projecting to C2 and L2 using Cre-dependent HSVs injected bilaterally.

(K) Left: transverse section (representative of 3 mice) at the rostrocaudal level 3 showing C2- (GFP) and L2-projecting (mCherry) V2a RS neurons. Scale bar, 500 μm. Insets to the right are magnifications of the blue boxed area, showing the scarcity of double-labeled neurons (open arrowheads). Scale bar, 100 μm.

(L) Bar graphs showing, at the 4 rostrocaudal levels, the average number ± SEM per histological section of V2a RS neurons projecting to either or both of the C2 and L2 segments (n = 3 mice; 844 cells counted in total; average cells per animal, 281 ± 33).

(M) Pie graphs showing the distribution, at rostrocaudal levels 2 and 3, of labeled neurons within the indicated subnuclei (in percent of all neurons at each level, pooled from the 3 mice). All cells at level 1 were in the MdV and all cells at level 4 were in the PnC.

(N) Left: transverse position of single- and double-labeled neurons at rostrocaudal level 3 where optogenetic activations are performed. Middle and right: mediolateral (in mm from the midline, absolute values from the left and the right sides are pooled) and dorsoventral (in mm from the ventral border) positions of single- and double-labeled neurons, presented as the mean (crosses) and box-and-whisker plots, which give the median, 25th and 75th percentiles, and range (844 cells pooled from 3 mice). **$p < 0.01$; ns, not significant (unpaired t test). See also Figures S4 and S5.

Please cite this article in press as: Usseglio et al., Control of Orienting Movements and Locomotion by Projection-Defined Subsets of Brainstem V2a Neurons, Current Biology (2020), https://doi.org/10.1016/j.cub.2020.09.014

CellPress
OPEN ACCESS

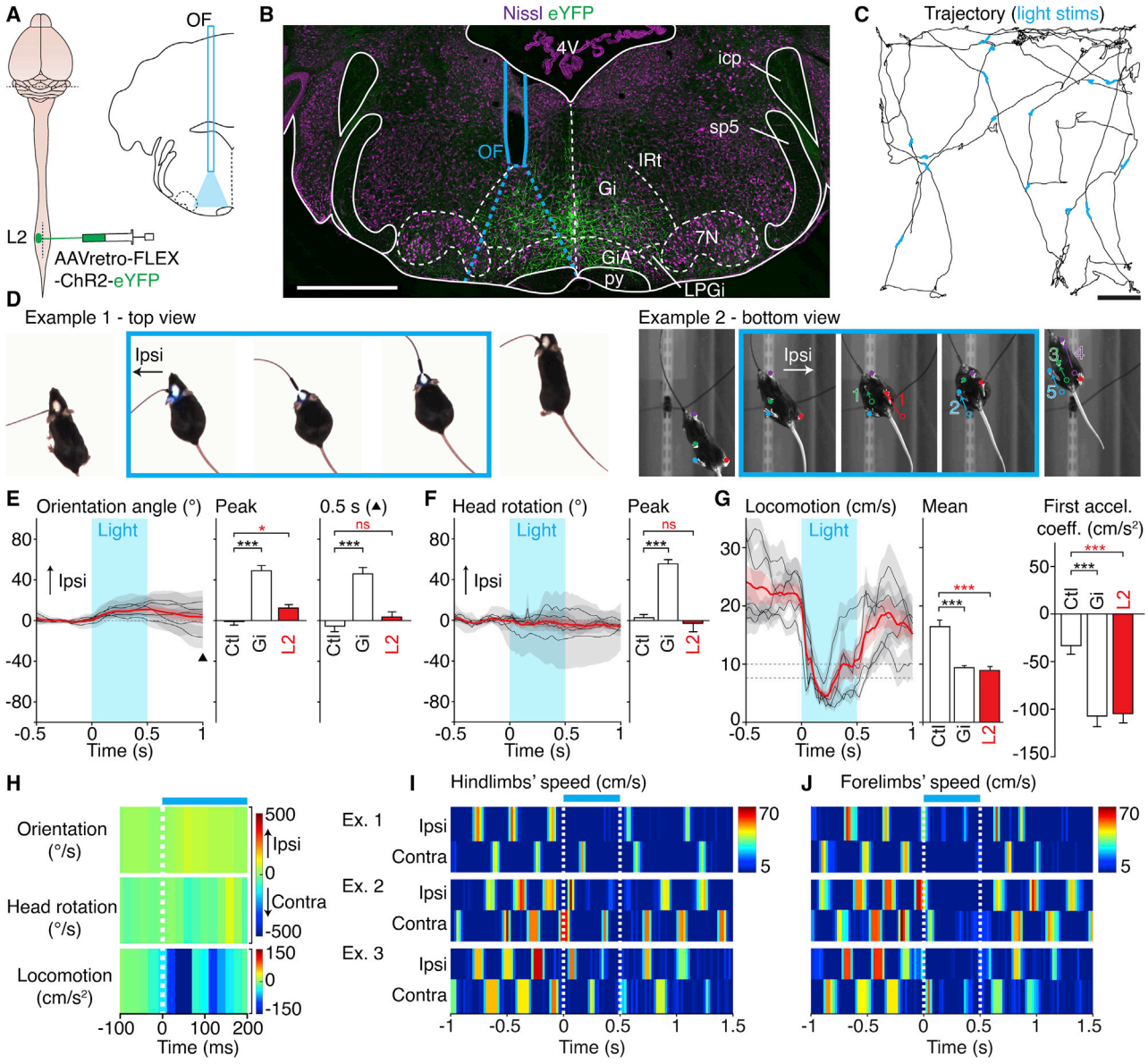

Figure 5. Unilateral Photo-Activations of L2-Projecting V2a Gi Neurons Arrest but Do Not Steer Ongoing Locomotion

(A) Experimental strategy for photo-activating L2-projecting V2a Gi neurons. OF, optic fiber.

(B) Example transverse section showing virally transfected V2a neurons (eYFP) on a Nissl background, the position of the optic fiber (OF), and the theoretical light cone at the fiber tip (dashed blue lines) that restricts activations to the implanted side. Scale bar, 1 mm. See also Figure S1D.

(C) Trajectory of one representative animal for 3 min in the open field. Scale bar, 10 cm.

(D) Example snapshots from two distinct animals, showing the locomotor arrest with no change in trajectory evoked by 500 ms light trains (15 ms pulses at 40 Hz, in blue) delivered unilaterally on the left side. Snapshots are taken 150 ms before light onset; 50 ms, 250 ms, and 450 ms after light onset; and 200 ms after light offset. See also Video S4.

(E–G) Left: mean ± SEM light-evoked changes in body orientation (E), head yaw rotation (F), and locomotor speed (G) of each animal (gray, n = 5 mice, 8 trials each) and across animals (red). The black arrowhead in (E) indicates the time point at 0.5 s after light offset. The dashed zone in (G) indicates the threshold from stationary (<7.5 cm/s) to locomoting (>10 cm/s) conditions. Bar graphs to the right show, for each parameter, the mean ± SEM of all trials when activating L2-projecting V2a neurons (in red, n = 40 trials from 5 mice, 8 trials each) compared with the same measurement in mock trials in control mice (Ctl, n = 48 trials from 4 mice, 12 trials each) and following activation of all V2a Gi neurons (Gi, n = 48 trials from 6 mice, 8 trials each). ***p < 0.001; *p < 0.05; ns, not significant (unpaired t test).

(legend continued on next page)

Please cite this article in press as: Usseglio et al., Control of Orienting Movements and Locomotion by Projection-Defined Subsets of Brainstem V2a Neurons, Current Biology (2020), https://doi.org/10.1016/j.cub.2020.09.014

V2a subsets contacted by the SC but that differ by their segmental projections to the spinal cord.

Differential Control of Head and Hindlimb Movements by Subsets of V2a Gi Neurons

The existence of projection-defined subsets of V2a Gi neurons prompted us to test their respective function. For this, a cre-dependent ChR2 was delivered retrogradely by unilateral injections of an AAVretro-FLEX-ChR2-eYFP [47–49] in the C2 or L2 spinal segments and an optic fiber was placed in the Gi on the same side. Since left-right unbalanced activation of lumbar circuits could steer trajectory [7, 8, 35], we first manipulated the L2-projecting V2a neurons (Figures 5A and 5B; see Figure S1D for implantation sites). Most surprisingly, however, their unilateral activation during locomotion did not change the animals' trajectory (Figures 5C and 5D; Video S4). Specifically, the animal's body orientation only showed a slight and transient bias that was not maintained after light offset (Figure 5E). Animals also did not show any head yaw rotation movements (Figures 5D and 5F). Locomotor speed was nevertheless strongly reduced similarly to the activation of all V2a Gi neurons: animals reached the stationary threshold on average 70 ± 17 ms after light onset (Figures 5D and 5G) and locomotor deceleration peaked at 40 ms after light onset (Figure 5H). Bottom-view examinations revealed that both hindlimbs and forelimbs were halted and positioned symmetrically (Figures 5D, 5I, and 5J; Video S4). On stationary animals, photo-stimulations did not evoke detectable changes in these motor parameters (Figures S6A–S6G and S6O). Hence, L2-projecting V2a neurons, when activated unilaterally, arrest locomotion but do not evoke head and orofacial orienting responses, nor steer trajectory.

The directional change evoked when activating V2a Gi neurons collectively might thus be driven by the C2-projecting subset. Indeed, when ChR2 was retrogradely delivered from the C2 segment and photo-activations performed in the Gi unilaterally during locomotion (Figures 6A and 6B; see Figure S1E for implantation sites), we observed a pronounced change in trajectory toward the stimulated side (Figures 6C and 6D; Video S5). Reminiscent of what we observed when activating V2a neurons collectively, the change in body orientation was highly significant from mock trials in control mice, persisted after light offset (Figure 6E), and was preceded by a rapid rotation of the head (Figure 6F). Remarkably, however, animals did not arrest their locomotion. Specifically, while a locomotor deceleration was observed, it was comparable to that of control mice subjected to mock trials (Figure 6G; see also Figure S2K for the responses of control mice). This ChR2-independent deceleration reflects the limited size of open field, which makes running episodes inevitably short, even in the absence of photo-activation. This locomotor deceleration also occurred later following light onset than when activating all V2a Gi neurons or the L2-projecting ones (Figure 6H; compare with Figures 5H and 3G), suggesting that it is not a primary response from photo-activations. Indeed left-right alternating movements of both hindlimbs and forelimbs persisted during the directional change (Figures 6D, 6I, and 6J; Video S5). Photo-activations on still trials evoked a strong yaw rotation of the head and a re-orientation of the body, and animals could perform a few walking steps toward the stimulated side; there was, however, no deflection of the snout (Figures S6H–S6O). Finally, we excluded a contribution of antidromic activation of C2-located V2a neurons with projections to the brainstem (Figure S7) and found no projections in the reticular formation from Chx10-expressing neurons located in L2 (data not shown). Overall, these results indicate that (1) the C2- and L2-projecting subsets of V2a Gi neurons are specifically dedicated to control head rotation and locomotor speed, respectively, and (2) the former action suffices to steer the animal's trajectory. They also suggest the existence of other V2a Gi neurons with no spinal projections that may control orofacial musculature.

C2-Projecting, but Not L2-Projecting, V2a Neurons Elicit Short-Latency Responses on Neck Muscle Fibers

Since our results underscore the importance of head rotation for locomotor trajectory and since neck premotor circuits reside in the Gi [20–22], we hypothesized that some V2a Gi neurons might be connected to neck motoneurons. We therefore recorded, by electromyography in non-anesthetized awake mice, photo-evoked responses of the splenius muscle, the most vigorously activated during horizontal orienting head movements [20, 50] (Figure 7).

Only animals showing spontaneous activity on both the ipsilateral and contralateral muscles (Figures 7B, 7F, and 7J) were included. When V2a Gi neurons were activated collectively by short (5 ms) light pulses, reliable EMG responses were detected on the ipsilateral side in nearly all trials (Figures 7C and 7D). These occurred at an average latency of 5.57 ± 0.13 ms (min, 3.8 ms; max, 6.8 ms) compatible with the crossing of 2 synapses [51–53]. However contralateral responses were less reliable and significantly more delayed (14.64 ± 0.96 ms, min, 9.6 ms; max, 25 ms). Photo-activating C2-projecting V2a neurons also led short responses ipsilaterally (latency, 6.13 ± 0.10 ms), but not contralaterally (10.74 ± 0.66 ms; Figures 7E–7H). In stark contrast, only occasional responses were observed both ipsilaterally and contralaterally when activating the L2-projecting subset (Figures 7I–7L), and when a response was elicited, its latency was longer on both sides (ipsilateral, 18.39 ± 0.63 ms, min 13.4 ms, max 24.4 ms; contralateral, 19.65 ± 0.65 ms, min 15.6 ms; max 25 ms). Finally, examination of anterograde projections of V2a Gi neurons in the upper cervical spinal cord revealed putative contacts onto motoneurons (Figures 7M and 7N). Overall, these experiments reinforce the existence of distinct functional V2a

(H) Color plot showing the temporal evolution of the motor parameters from 100 ms before to 200 ms after light onset (the dashed white line indicates light onset). Note the absence of trajectory change and head rotation, but a rapid locomotor deceleration (peak at 40 ms) reminiscent of activating V2a Gi neurons collectively (Figure 3G).

(I and J) Color plots of the velocity of the paws of the hindlimbs (I) and forelimbs (J) from 1 s before to 1 s after the photo-activation. A color gradient to red indicates high speed values in cm/s. The y axis represents 3 example trials from distinct animals. The second one corresponds to the snapshots in (D). See also Figure S2 for the responses of control mice and Figure S6 for still trials.

Please cite this article in press as: Usseglio et al., Control of Orienting Movements and Locomotion by Projection-Defined Subsets of Brainstem V2a Neurons, Current Biology (2020), https://doi.org/10.1016/j.cub.2020.09.014

CellPress
OPEN ACCESS

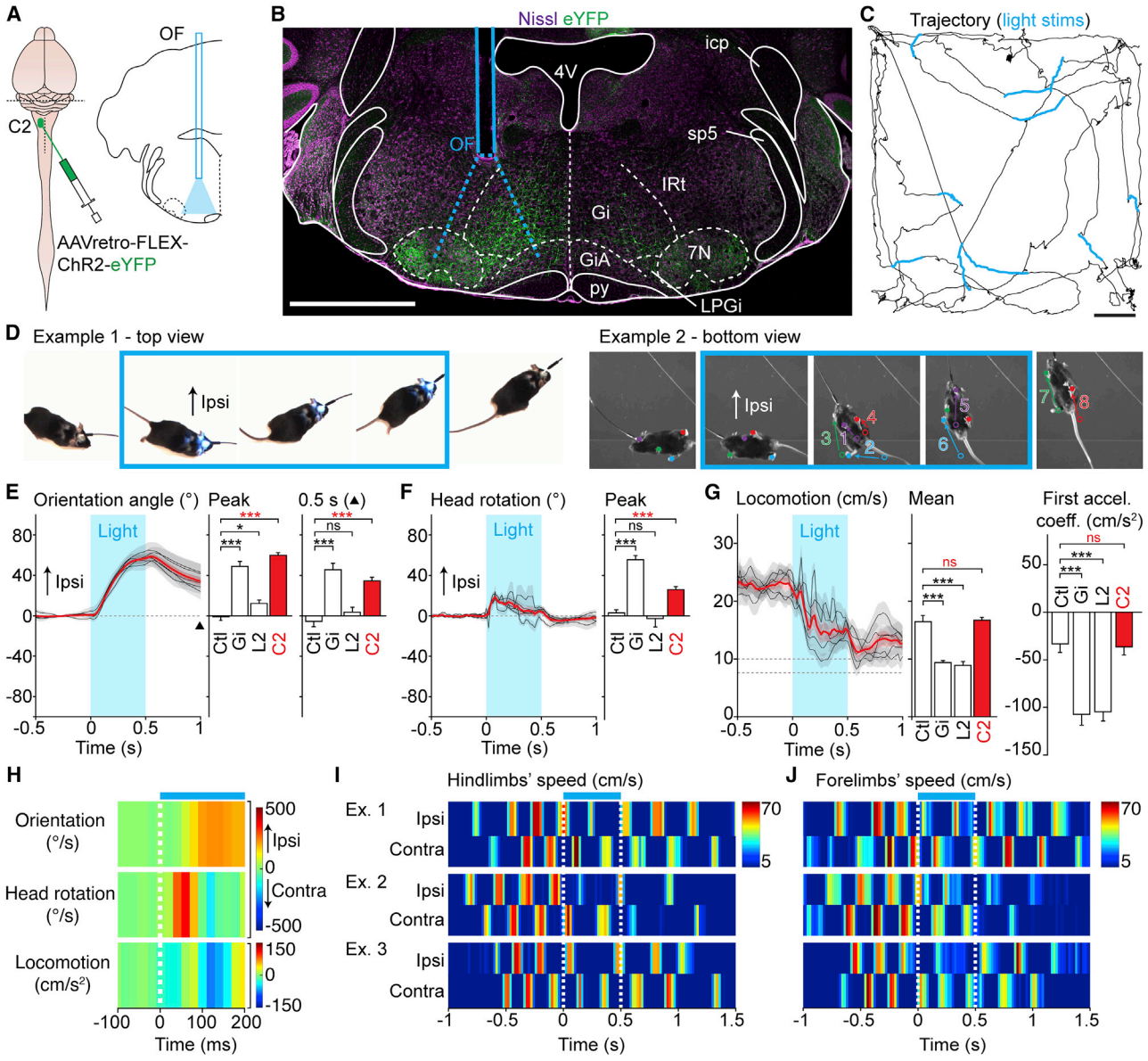

Figure 6. Unilateral Photo-Activations of C2-Projecting V2a Gi Neurons Steer, but Do Not Arrest, Ongoing Locomotion

(A) Experimental strategy for photo-activating C2-projecting V2a Gi neurons. OF, optic fiber.

(B) Example transverse section showing virally transfected V2a neurons (eYFP) on a Nissl background, the position of the optic fiber (OF), and the theoretical light cone at the fiber tip (dashed blue lines) that restricts activations to the implanted side. Scale bar, 1 mm. See also Figure S1E.

(C) Trajectory of one representative animal during 3 min in the open field. Scale bar, 10 cm.

(D) Example snapshots from two distinct animals, showing the change in trajectory without locomotor arrest, evoked by 500 ms light trains (15 ms pulses at 40 Hz, in blue). Snapshots are taken 150 ms before light onset; 50 ms, 250 ms, and 450 ms after light onset; and 200 ms after light offset. See also Video S5.

(E–G) Left: mean ± SEM light-evoked changes in body orientation (E), head yaw rotation (F), and locomotor speed (G) of each animal (gray, n = 5 mice, 23 trials each) and across animals (red). The black arrowhead in (E) indicates the time point at 0.5 s after light offset. The dashed zone in (G) indicates the threshold from stationary (<7.5 cm/s) to locomoting (>10 cm/s) conditions. Bar graphs to the right show, for each parameter, the mean ± SEM obtained across all trials when activating C2-projecting V2a neurons (in red, n = 115 trials from 5 mice, 23 trials each) compared with the same measurement in mock trials in control mice (Ctl, n = 48 trials from 4 mice, 12 trials each) and following activation of all V2a Gi neurons (Gi, n = 48 trials from 6 mice, 8 trials each) or the L2-projecting ones (L2, n = 40 trials from 5 mice, 8 trials each). ***p < 0.001; *p < 0.05; ns, not significant (unpaired t test).

(H) Color plot showing the temporal evolution of motor parameters from 100 ms before to 200 ms after light onset (the dashed white line indicates light onset). Note the rapid head rotation (peak at 60 ms) and the delayed body orientation (peak at 120 ms), but the absence of rapid deceleration of locomotion.

(I and J) Color plots of the velocity of the paws of the hindlimbs (I) and forelimbs (J) from 1 s before to 1 s after the photo-activations. A color gradient to red indicates high speed values in cm/s. The y axis represents 3 example trials from distinct animals. The first example corresponds to the snapshots in (D). See also Figure S2 for the responses of control mice and Figure S6 for still trials.

Please cite this article in press as: Usseglio et al., Control of Orienting Movements and Locomotion by Projection-Defined Subsets of Brainstem V2a Neurons, Current Biology (2020), https://doi.org/10.1016/j.cub.2020.09.014

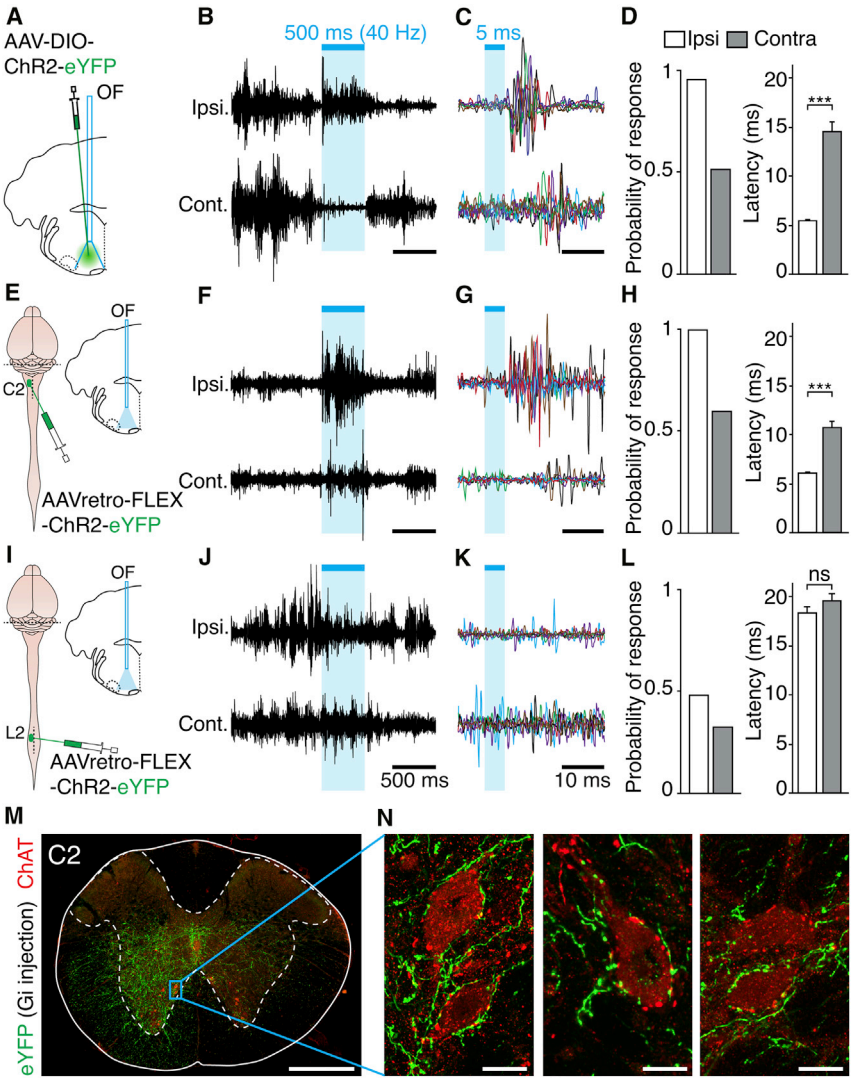

Figure 7. C2-Projecting V2a Neurons Elicit Short-Latency Responses on Neck Muscle Fibers

(A) Experimental strategy for photo-activating V2a Gi neurons. OF, optic fiber.

(B) Example EMG recording showing spontaneous activity on both the ipsilateral and contralateral neck muscles, and the increased activity ipsilaterally following photo-activation of V2a Gi neurons (15 ms pulses at 40 Hz, for a duration of 500 ms).

(C) Six superimposed EMG traces following a single 5 ms light pulse, each shown in a specific color.

(D) Bar graphs showing the presence of reliable (95% success) and low-latency responses (mean, 5.6 ± 0.1 ms; min, 3.8; max, 6.8) ipsilaterally, but not contralaterally (51% success; mean, 14.7 ± 1.0 ms; min, 9.6; max, 25). ***$p < 0.001$ (unpaired t test on n = 68 trials from 3 mice). Data are presented as means across all trials; errors bars in the latency bar graph indicate SEM.

(E–H) Similar recordings and analyses for C2-projecting V2a neurons. Note the reliable and low-latency responses on the ipsilateral (100% success; mean, 6.1 ± 0.1 ms; min, 4.0; max, 8.0), but not on the contralateral muscle (60% success; mean, 10.7 ± 0.7 ms; min, 5.1; max, 19.6). ***$p < 0.001$ (unpaired t test on n = 62 trials from 3 mice).

(I–L) Similar recordings and analyses for L2-projecting V2a neurons. Note the low probability and long latency of responses on both the ipsilateral (48% success; mean, 18.4 ± 0.6 ms; min, 13.4; max, 24.4) and contralateral muscles (33% success; mean, 19.7 ± 0.7 ms; min, 15.6 ms; max, 25 ms). ns, not significant (unpaired t test on n = 78 trials from 4 mice).

(M) Confocal microscopy picture of a transverse section at C2 of an animal injected unilaterally in the Gi with an AAV-DIO-ChR2-EYFP (experimental individual illustrated in Figure 2B), showing anterograde V2a projections (eYFP) and motoneurons (ChAT). Scale bar, 500 μm.

(N) Left: higher magnification of the blue boxed area in (M), showing putative V2a contacts onto 2 motoneurons. The middle and right panels are other examples from the same (middle) and from another (right) animal. Scale bars, 20 μm.

subtypes with specialized projections, and indicate that the C2-projecting, but not the L2-projecting one, has rapid—possibly direct—access to neck motoneurons.

DISCUSSION

Methodological Considerations

A large part of our study relies on projection-based manipulations of neuronal subtypes. While retrogradely transported HSV and AAVretro vectors have already proven to be extremely powerful tools [45, 47–49], notably owing to their restricted entry at terminals [45, 54, 55], there are potential concerns that deserve clarification. First, if wild HSVs can prevent a single cell from being infected by multiple viruses [56], the replication-deficient ones used here are deprived of viral genome [44] and allow multiple infections [46] (Figure S4). Furthermore, little co-labeling was also observed when combining an HSV injection at C2 with CTB at L2 (Figures 4F–4I), unambiguously ascertaining that distinct V2a neurons contact the cervical and lumbar segments. Another concern with dual injections is the risk of severing axons at the rostral site, which can cause an underestimation of neurons projecting more caudally. However, here, all spinal injections were done starting from the lumbar site and performed in the white matter to spare the lateral funiculus where most RS axons travel [19], and animals showed no motor deficits. Furthermore, the existence of distinct V2a subsets is not only supported anatomically but is also demonstrated functionally. Indeed, following a unique injection of a ChR2-coding AAVretro in the L2 segment, i.e., without possible axonal damage at the cervical level, no head movements or short-latency EMG responses on neck muscle fibers were detected (Figures 5 and 7). V2a neurons transfected from L2 therefore do not have a similar access to cervical segments as the overall population or the C2-projecting ones. Finally, the contribution of antidromic activation of spinally located

Please cite this article in press as: Usseglio et al., Control of Orienting Movements and Locomotion by Projection-Defined Subsets of Brainstem V2a Neurons, Current Biology (2020), https://doi.org/10.1016/j.cub.2020.09.014

V2a neurons with projections to the brainstem can be ruled out since (1) motor actions evoked after retrograde delivery of ChR2 are seen when manipulating V2a Gi neurons locally, i.e., without the possibility for distant V2a neurons to express ChR2; (2) activating ascending projections of V2a neurons residing in C2 led to no orienting responses (Figure S7); and (3) Chx10-expressing neurons in L2 do not project to the RF. Overall, the selectivity and convergence of our anatomical (HSV) and functional (AAVretro) investigations firmly establish the existence of distinct functional V2a subsets with preferential projections to the upper cervical or lumbar segments.

The Presynaptic Connectome of V2a Gi Neurons Hints at Their Integrative Function

Aside from the dominant local connectivity, a high fraction of presumed inputs to V2a Gi neurons was found in the SC, in positions matching the output layers known to project to the RF [12, 15]. The majority of SC output neurons are excitatory and the ipsilateral orienting responses we observed are reminiscent of those elicited contralaterally when activating the SC [14, 42]. This suggests that V2a Gi neurons are embedded in an excitatory crossed pathway, as also indicated by a coincident and independent investigation [35]. Interestingly, we found that the SC contacts both the C2- and L2-projecting V2a subsets. Therefore, the latter, while not directly mediating lateralized motor actions, may still relay orientation-related signals. Indeed, the animal's locomotor speed is often encoded together with its directional heading [57, 58], suggesting a tight correlation of these two variables. Allowing a transient arrest of locomotion appears notably pertinent for exploring a fixed object while on the move. Alternatively, the SC projections to L2-projecting V2a neurons may be related to defensive behaviors, also manifested by a behavioral arrest [59]. The role and excitatory or inhibitory nature of the uncrossed pathway from the SC to V2a neurons, less predominant, will need to be uncovered. Finally, the detection of transneuronally labeled neurons in other brain regions known to regulate motor actions or posture [60–62] indicates that V2a Gi neurons may be shared by several modalities that require spatially tuned movements. Here again, examining the neurotransmitter identity of these upstream neurons will be required to fully appreciate their role in mobilizing or inactivating V2a Gi neurons. However, we found no transneuronal labeling in the cuneiform and pedunculopontine nuclei, together forming the mesencephalic locomotor region (MLR) that engages forward locomotion [40, 41]. This could reflect that forward locomotion may be, at least in mice, principally controlled by non-V2a glutamatergic or serotonergic neuronal classes [26, 63]. However, MLR to V2a connections have been suggested functionally *in vitro* [36]. These connections may thus target V2a neurons not investigated here (notably located more caudally) or may be more refractory to rabies transfer.

Differential Control of Head and Hindlimb Movements by Subsets of V2a Neurons

We report here that V2a Gi neurons trigger both "strict" orienting responses ipsilaterally, i.e., lateralized head and orofacial movements, and steer trajectory when activated during locomotion. Conversely, ablating or silencing V2a Gi neurons led to a biased contralateral turning during exploration, in line with a coincident and independent investigation [35]. Such opposite findings from gain and loss of functions exclude that photo-evoked responses owe to an unintentional suppression of activity by over-activation, as previously ruled out for the locomotor aspect [34]. Most importantly, they strongly argue that V2a Gi neurons might be mobilized during—and are causal to—naturally occurring changes of direction. Interestingly, the bias in the head orientation suggests that these neurons might not only be transiently activated at turns, but may also help maintain an upright posture.

The V2a-driven directional change is associated with a bilateral arrest of the hindlimbs, which is reminiscent (i.e., gradual, leading to a stereotypic stationary posture) of what was previously reported when activating the same cells bilaterally [34]. Remarkably, however—and this is certainly the most disruptive finding reported here—the directional change and the locomotor halt are in fact controlled by distinct V2a populations with segment-specific projections. This specialization of V2a neurons is demonstrated both anatomically (Figures 4 and S4) and functionally (Figures 5, 6, 7, and S6). Specifically, activating C2-projecting V2a neurons led to an ipsilateral head yaw rotation followed by a change in trajectory but no locomotor arrest, suggesting that this population does not reach or functionally impact hindlimb-related segments. While these C2-projecting V2a neurons were inevitably activated in previous work [34], their function may have then been hindered by the bilateral nature of the stimulations that may have caused left-right co-contractions of neck muscles (but see [26] for head movements when photo-activating glutamatergic Gi neurons). Conversely, we report a rapid locomotor arrest, but no head rotation, short neck EMG responses, or directional change, when activating L2-projecting V2a neurons (Figures 5 and S6). Therefore, L2-projecting V2a neurons do not reach or functionally impact neck-related cervical segments. Even though our retrograde approach transfects somata on both sides since V2a Gi neurons have crossed projections (Figures 4C–4E), the locomotor halt cannot be due to an unintentional synchronous activation of the left and right sides since (1) the lateral placement of the optic fiber secures unilateral photo-activations [64], and (2) a bilateral arrest is systematically evoked when the ChR2 is delivered locally and unilaterally to the Gi (Figure 3), where there is no possible activation of neurons located across the midline (Figure S1A). This diversification of descending neurons by targeted segment is reminiscent to what was recently uncovered for cerebello-spinal neurons [49]. However, here, we highlight a salt and pepper, body-oriented functional organization at the connectomics levels rather than a spatial topography. While we also detected a numerically smaller subset of V2a neurons with projections to both spinal segments, it is unlikely that it controls head and limb movements synergistically since activating the L2- and C2-projecting subsets evoked mutually exclusive responses. Finally, nose movements were only observed when activating V2a Gi neurons collectively. The snout musculature may thus be controlled by yet another population with only local projections [17]. Therefore, and considering that some brainstem V2a neurons may also modulate breathing [32], this neuronal class appears heterogeneous and may host projection-specialized subsets that each control a specific muscle group.

Please cite this article in press as: Usseglio et al., Control of Orienting Movements and Locomotion by Projection-Defined Subsets of Brainstem V2a Neurons, Current Biology (2020), https://doi.org/10.1016/j.cub.2020.09.014

The Head Orientation as a Prime Driver for Locomotor Trajectory?

On the role of V2a neurons on locomotor trajectory, we converge with a coincident work by Cregg et al. [35]. However, in this independent study, V2a Gi neurons were only manipulated collectively, i.e., regardless of their efferent connectivity. Consequently, our conclusions on the implicated circuits diverge. Cregg et al. propose that locomotor trajectory changes owe to a depression of hindlimb circuits and movements on the side of activated V2a descending neurons. This implies that a unique V2a population steers locomotion when mobilized unilaterally and halts it when mobilized bilaterally. Instead we establish here that the directional change and the locomotor halt are controlled by distinct V2a subsets that differ by their segmental projections and can therefore be experimentally manipulated independently. Our work altogether argues that the impact of V2a Gi neurons on locomotor trajectory is rather primarily supported by their capacity to impose the head orientation. In fact, the head rotation precedes the trajectory changes evoked experimentally (Figure 3G) or occurring spontaneously (Figure S3) and has been postulated as a prime driver for locomotor trajectory in humans [4–6]. In swimming species, trajectory changes are also initiated by a bending of the head and trunk [13]. Our work hence highlights the importance of the head in directing movement path across species. To be clear, we do not dispute that activating V2a Gi neurons collectively—or the C2-projecting subset selectively—leads to asymmetric limb movements [35] (Figures 3H and 6D). Yet we show here that this asymmetry does not appear to be a primary consequence of activated descending V2a neurons reaching the hindlimb controllers in the lumbar spinal cord. It may rather be an adaptive adjustment to the displacement of the body axis, primed by the head (and possibly the forelimbs), which *is* driven by C2-projecting V2a Gi neurons. Changes in body orientation can in fact be imposed by activating V2a neurons on stationary animals (Figures 2C–2E, S6I, and S6J). How such displacement translates in an asymmetric limb pattern while on the move remains to be determined. Limb sensory inputs can adjust stance patterns during mechanically forced directional changes [65, 66] and should notably be examined.

Limitations

Our opposite findings from gain and loss of function indicate that V2a neurons' activity is both causal to, and required for, head orientating movements and trajectory changes. Our results, however, do not speak to whether V2a neurons are mobilized during natural behaviors and at all situations that need oriented movements. Interestingly, natural turnings can be, but do not have to be, associated with a locomotor arrest (Figure S3), suggesting that each subtype could even be recruited independently. Head-mounted microscopes [67] should be considered in future experiments with some developments to overcome the sparsity and deep location of the V2a population. Another intriguing finding reported here is that the two V2a subsets evoke opposing actions: motor excitation for the C2-projecting one, functional inhibition for the L2-projecting one. Yet V2a neurons at all positions of the medullary RF are glutamatergic and do not co-express inhibitory or serotonergic markers [34, 36]. The functional outcome of each subset may therefore owe to the cell types contacted in the spinal cord. Admittedly, we have not examined V2a targets in detail, but the short-latency responses on neck muscles and the putative contacts on cervical motoneurons (Figure 7) raise the possibility that V2a RS neurons may include neck premotoneurons [20, 22]. V2a neurons can indeed be premotoneurons, at least in the spinal cord [68, 69]. Dedicated tracings from muscles [70] will be needed to ascertain this possibility in the brainstem. Instead, the L2-projecting subset may correspond to the previously identified V2a "stop neurons" and may depress locomotor circuits indirectly via inhibitory spinal neurons [34], whose activation can halt locomotion [71]. Characterizing the V2a postsynaptic targets will therefore be extremely informative and should now be achievable with anterograde transneuronal vectors [72]. Finally, while we focused on the rostral medulla (i.e., levels encompassing the Gi and GiA), V2a neurons located more caudally also project to the spinal cord (Figures 4I and 4L) and their function will need to be determined.

General Conclusion

Our work has identified subtypes of reticular neurons that are downstream of the superior colliculus and that control multiple motor actions pertinent for orientation. These subtypes share a common genetic identity and anatomical positioning, but differ by their efferent connectivity. Our study therefore underscores the organization of the reticular formation in functional modules defined by transcription factors, and at the same time argues for a further segregation within modules whereby a functional connectivity organized by muscles or muscle groups may underlie the execution of individual motor actions of a coherent behavior. This represents an entry point to further decipher the neuronal basis for the diversity of motor repertoires and how the brain elaborates complex movements.

STAR★METHODS

Detailed methods are provided in the online version of this paper and include the following:

- KEY RESOURCES TABLE
- RESOURCE AVAILABILITY
  - Lead Contact
  - Materials Availability
  - Data and Code Availability
- EXPERIMENTAL MODEL AND SUBJECT DETAILS
  - Mice
  - Viruses used
- METHOD DETAILS
  - Surgical procedures for injections and implants in the brainstem
  - Surgical procedures for injections in the spinal cord
  - Histology
  - Delineation of brainstem structures and cellular counts
  - Behavioral experiments
  - Electromyographic Recordings
- QUANTIFICATION AND STATISTICAL ANALYSIS
  - Pose estimation using DeepLabCut and quantifications of body and head movements
  - Calculations of limb velocity

- Statistical analysis for optogenetic experiments
- Statistical analysis for ablation and silencing experiments
- Statistical analysis for electromyographic recordings

SUPPLEMENTAL INFORMATION

Supplemental Information can be found online at https://doi.org/10.1016/j.cub.2020.09.014.

ACKNOWLEDGMENTS

This work was funded by an Agence Nationale pour la Recherche grant (ANR-17-CE16-0027) to J.B. and by NeuroPSI, CNRS, and Université Paris-Saclay. G.U. holds a Université Paris-Saclay doctoral fellowship. C.H. holds doctoral fellowships from Région Ile-de-France and Fondation pour la Recherche Médicale. We thank Séverine Diem for assistance with genotyping, Tihana Jovanic for critical reading of the manuscript, and Beatrice Cerocchi for the mouse drawings in the graphical abstract. Other schematics are from Scidraw.io.

AUTHOR CONTRIBUTIONS

J.B. designed the study and supervised the work. G.U. performed experiments with contributions from J.B. and A.H. and analyzed anatomical data. E.G. designed tracking scripts and analyzed the behavioral data with J.B. C.H. helped establish and performed initial transneuronal tracings. G.U. and J.B. prepared figures. J.B. wrote the paper and all authors contributed to its editing.

DECLARATION OF INTERESTS

The authors declare no competing interests.

Received: April 1, 2020
Revised: August 3, 2020
Accepted: September 4, 2020
Published: October 1, 2020

REFERENCES

1. Mitchinson, B., and Prescott, T.J. (2013). Whisker movements reveal spatial attention: a unified computational model of active sensing control in the rat. PLoS Comput. Biol. *9*, e1003236.
2. Kurnikova, A., Moore, J.D., Liao, S.M., Deschênes, M., and Kleinfeld, D. (2017). Coordination of orofacial motor actions into exploratory behavior by rat. Curr. Biol. *27*, 688–696.
3. Guitton, D. (1992). Control of eye-head coordination during orienting gaze shifts. Trends Neurosci. *15*, 174–179.
4. Grasso, R., Glasauer, S., Takei, Y., and Berthoz, A. (1996). The predictive brain: anticipatory control of head direction for the steering of locomotion. Neuroreport *7*, 1170–1174.
5. Dollack, F., Perusquía-Hernández, M., Kadone, H., and Suzuki, K. (2019). Head anticipation during locomotion with auditory instruction in the presence and absence of visual input. Front. Hum. Neurosci. *13*, 293.
6. Grasso, R., Prévost, P., Ivanenko, Y.P., and Berthoz, A. (1998). Eye-head coordination for the steering of locomotion in humans: an anticipatory synergy. Neurosci. Lett. *253*, 115–118.
7. Oueghlani, Z., Simonnet, C., Cardoit, L., Courtand, G., Cazalets, J.R., Morin, D., Juvin, L., and Barrière, G. (2018). Brainstem steering of locomotor activity in the newborn rat. J. Neurosci. *38*, 7725–7740.
8. Fagerstedt, P., and Ullén, F. (2001). Lateral turns in the lamprey. I. Patterns of motoneuron activity. J. Neurophysiol. *86*, 2246–2256.
9. Basso, M.A., and May, P.J. (2017). Circuits for action and cognition: a view from the superior colliculus. Annu. Rev. Vis. Sci. *3*, 197–226.
10. Song, J.H., Rafal, R.D., and McPeek, R.M. (2011). Deficits in reach target selection during inactivation of the midbrain superior colliculus. Proc. Natl. Acad. Sci. USA *108*, E1433–E1440.
11. Stubblefield, E.A., Costabile, J.D., and Felsen, G. (2013). Optogenetic investigation of the role of the superior colliculus in orienting movements. Behav. Brain Res. *255*, 55–63.
12. Felsen, G., and Mainen, Z.F. (2008). Neural substrates of sensory-guided locomotor decisions in the rat superior colliculus. Neuron *60*, 137–148.
13. Saitoh, K., Ménard, A., and Grillner, S. (2007). Tectal control of locomotion, steering, and eye movements in lamprey. J. Neurophysiol. *97*, 3093–3108.
14. Sahibzada, N., Dean, P., and Redgrave, P. (1986). Movements resembling orientation or avoidance elicited by electrical stimulation of the superior colliculus in rats. J. Neurosci. *6*, 723–733.
15. Sparks, D.L., and Hartwich-Young, R. (1989). The deep layers of the superior colliculus. Rev. Oculomot. Res. *3*, 213–255.
16. Redgrave, P., Mitchell, I.J., and Dean, P. (1987). Descending projections from the superior colliculus in rat: a study using orthograde transport of wheatgerm-agglutinin conjugated horseradish peroxidase. Exp. Brain Res. *68*, 147–167.
17. Kleinfeld, D., Moore, J.D., Wang, F., and Deschenes, M. (2014). The brainstem oscillator for whisking and the case for breathing as the master clock for orofacial motor actions. Cold Spring Harb. Symp. Quant. Biol. *79*, 29–39.
18. Sparks, D.L. (2002). The brainstem control of saccadic eye movements. Nat. Rev. Neurosci. *3*, 952–964.
19. Liang, H., Watson, C., and Paxinos, G. (2016). Terminations of reticulospinal fibers originating from the gigantocellular reticular formation in the mouse spinal cord. Brain Struct. Funct. *221*, 1623–1633.
20. Isa, T., and Sasaki, S. (2002). Brainstem control of head movements during orienting; organization of the premotor circuits. Prog. Neurobiol. *66*, 205–241.
21. Sasaki, S., Yoshimura, K., and Naito, K. (2004). The neural control of orienting: role of multiple-branching reticulospinal neurons. Prog. Brain Res. *143*, 383–389.
22. Peterson, B.W., Pitts, N.G., Fukushima, K., and Mackel, R. (1978). Reticulospinal excitation and inhibition of neck motoneurons. Exp. Brain Res. *32*, 471–489.
23. Kiehn, O. (2016). Decoding the organization of spinal circuits that control locomotion. Nat. Rev. Neurosci. *17*, 224–238.
24. Grillner, S., and El Manira, A. (2020). Current principles of motor control, with special reference to vertebrate locomotion. Physiol. Rev. *100*, 271–320.
25. Jordan, L.M., Liu, J., Hedlund, P.B., Akay, T., and Pearson, K.G. (2008). Descending command systems for the initiation of locomotion in mammals. Brain Res. Brain Res. Rev. *57*, 183–191.
26. Capelli, P., Pivetta, C., Soledad Esposito, M., and Arber, S. (2017). Locomotor speed control circuits in the caudal brainstem. Nature *551*, 373–377.
27. Kim, L.H., Sharma, S., Sharples, S.A., Mayr, K.A., Kwok, C.H.T., and Whelan, P.J. (2017). Integration of descending command systems for the generation of context-specific locomotor behaviors. Front. Neurosci. *11*, 581.
28. Ferreira-Pinto, M.J., Ruder, L., Capelli, P., and Arber, S. (2018). Connecting circuits for supraspinal control of locomotion. Neuron *100*, 361–374.
29. Isa, T., and Sasaki, S. (1988). Effects of lesion of paramedian pontomedullary reticular formation by kainic acid injection on the visually triggered horizontal orienting movements in the cat. Neurosci. Lett. *87*, 233–239.
30. Li, S., Misra, K., Matise, M.P., and Xiang, M. (2005). Foxn4 acts synergistically with Mash1 to specify subtype identity of V2 interneurons in the spinal cord. Proc. Natl. Acad. Sci. USA *102*, 10688–10693.
31. Briscoe, J., and Ericson, J. (2001). Specification of neuronal fates in the ventral neural tube. Curr. Opin. Neurobiol. *11*, 43–49.

32. Crone, S.A., Viemari, J.C., Droho, S., Mrejeru, A., Ramirez, J.M., and Sharma, K. (2012). Irregular breathing in mice following genetic ablation of V2a neurons. J. Neurosci. *32*, 7895–7906.

33. Kimura, Y., Satou, C., Fujioka, S., Shoji, W., Umeda, K., Ishizuka, T., Yawo, H., and Higashijima, S. (2013). Hindbrain V2a neurons in the excitation of spinal locomotor circuits during zebrafish swimming. Curr. Biol. *23*, 843–849.

34. Bouvier, J., Caggiano, V., Leiras, R., Caldeira, V., Bellardita, C., Balueva, K., Fuchs, A., and Kiehn, O. (2015). Descending command neurons in the brainstem that halt locomotion. Cell *163*, 1191–1203.

35. Cregg, J.M., Leiras, R., Montalant, A., Wanken, P., Wickersham, I.R., and Kiehn, O. (2020). Brainstem neurons that command mammalian locomotor asymmetries. Nat. Neurosci. *23*, 730–740.

36. Bretzner, F., and Brownstone, R.M. (2013). Lhx3-Chx10 reticulospinal neurons in locomotor circuits. J. Neurosci. *33*, 14681–14692.

37. Kim, E.J., Jacobs, M.W., Ito-Cole, T., and Callaway, E.M. (2016). Improved monosynaptic neural circuit tracing using engineered rabies virus glycoproteins. Cell Rep. *15*, 692–699.

38. Azim, E., Jiang, J., Alstermark, B., and Jessell, T.M. (2014). Skilled reaching relies on a V2a propriospinal internal copy circuit. Nature *508*, 357–363.

39. Romer, S.H., Seedle, K., Turner, S.M., Li, J., Baccei, M.L., and Crone, S.A. (2017). Accessory respiratory muscles enhance ventilation in ALS model mice and are activated by excitatory V2a neurons. Exp. Neurol. *287*, 192–204.

40. Caggiano, V., Leiras, R., Goñi-Erro, H., Masini, D., Bellardita, C., Bouvier, J., Caldeira, V., Fisone, G., and Kiehn, O. (2018). Midbrain circuits that set locomotor speed and gait selection. Nature *553*, 455–460.

41. Josset, N., Roussel, M., Lemieux, M., Lafrance-Zoubga, D., Rastqar, A., and Bretzner, F. (2018). Distinct contributions of mesencephalic locomotor region nuclei to locomotor control in the freely behaving mouse. Curr. Biol. *28*, 884–901.e3.

42. Masullo, L., Mariotti, L., Alexandre, N., Freire-Pritchett, P., Boulanger, J., and Tripodi, M. (2019). Genetically defined functional modules for spatial orienting in the mouse superior colliculus. Curr. Biol. *29*, 2892–2904.e8.

43. Yang, C.F., Chiang, M.C., Gray, D.C., Prabhakaran, M., Alvarado, M., Juntti, S.A., Unger, E.K., Wells, J.A., and Shah, N.M. (2013). Sexually dimorphic neurons in the ventromedial hypothalamus govern mating in both sexes and aggression in males. Cell *153*, 896–909.

44. Neve, R.L., Neve, K.A., Nestler, E.J., and Carlezon, W.A., Jr. (2005). Use of herpes virus amplicon vectors to study brain disorders. Biotechniques *39*, 381–391.

45. Reinhard, K., Li, C., Do, Q., Burke, E.G., Heynderickx, S., and Farrow, K. (2019). A projection specific logic to sampling visual inputs in mouse superior colliculus. eLife *8*, e50697.

46. Coopersmith, R., and Neve, R.L. (1999). Expression of multiple proteins within single primary cortical neurons using a replication deficient HSV vector. Biotechniques *27*, 1156–1160.

47. Tervo, D.G., Hwang, B.Y., Viswanathan, S., Gaj, T., Lavzin, M., Ritola, K.D., Lindo, S., Michael, S., Kuleshova, E., Ojala, D., et al. (2016). A designer AAV variant permits efficient retrograde access to projection neurons. Neuron *92*, 372–382.

48. Ren, J., Friedmann, D., Xiong, J., Liu, C.D., Ferguson, B.R., Weerakkody, T., DeLoach, K.E., Ran, C., Pun, A., Sun, Y., et al. (2018). Anatomically defined and functionally distinct dorsal raphe serotonin sub-systems. Cell *175*, 472–487.e20.

49. Sathyamurthy, A., Barik, A., Dobrott, C.I., Matson, K.J.E., Stoica, S., Pursley, R., Chesler, A.T., and Levine, A.J. (2020). Cerebellospinal neurons regulate motor performance and motor learning. Cell Rep. *31*, 107595.

50. Roucoux, A., Crommelinck, M., and Decostre, M.F. (1989). Neck muscle activity in eye–head coordinated movements. Prog. Brain Res. *80*, 351–362, discussion 347–349.

51. Ueno, M., Nakamura, Y., Li, J., Gu, Z., Niehaus, J., Maezawa, M., Crone, S.A., Goulding, M., Baccei, M.L., and Yoshida, Y. (2018). Corticospinal circuits from the sensory and motor cortices differentially regulate skilled movements through distinct spinal interneurons. Cell Rep. *23*, 1286–1300.e7.

52. Maeda, H., Fukuda, S., Kameda, H., Murabe, N., Isoo, N., Mizukami, H., Ozawa, K., and Sakurai, M. (2016). Corticospinal axons make direct synaptic connections with spinal motoneurons innervating forearm muscles early during postnatal development in the rat. J. Physiol. *594*, 189–205.

53. Palmieri, R.M., Ingersoll, C.D., and Hoffman, M.A. (2004). The hoffmann reflex: methodologic considerations and applications for use in sports medicine and athletic training research. J. Athl. Train. *39*, 268–277.

54. McGavern, D.B., and Kang, S.S. (2011). Illuminating viral infections in the nervous system. Nat. Rev. Immunol. *11*, 318–329.

55. Antinone, S.E., and Smith, G.A. (2010). Retrograde axon transport of herpes simplex virus and pseudorabies virus: a live-cell comparative analysis. J. Virol. *84*, 1504–1512.

56. Criddle, A., Thornburg, T., Kochetkova, I., DePartee, M., and Taylor, M.P. (2016). gD-independent superinfection exclusion of alphaherpesviruses. J. Virol. *90*, 4049–4058.

57. Sargolini, F., Fyhn, M., Hafting, T., McNaughton, B.L., Witter, M.P., Moser, M.B., and Moser, E.I. (2006). Conjunctive representation of position, direction, and velocity in entorhinal cortex. Science *312*, 758–762.

58. Muzzu, T., Mitolo, S., Gava, G.P., and Schultz, S.R. (2018). Encoding of locomotion kinematics in the mouse cerebellum. PLoS ONE *13*, e0203900.

59. Shang, C., Chen, Z., Liu, A., Li, Y., Zhang, J., Qu, B., Yan, F., Zhang, Y., Liu, W., Liu, Z., et al. (2018). Divergent midbrain circuits orchestrate escape and freezing responses to looming stimuli in mice. Nat. Commun. *9*, 1232.

60. Murer, M.G., and Pazo, J.H. (1993). Circling behaviour induced by activation of GABAA receptors in the subthalamic nucleus. Neuroreport *4*, 1219–1222.

61. Supko, D.E., Uretsky, N.J., and Wallace, L.J. (1991). Activation of AMPA/kainic acid glutamate receptors in the zona incerta stimulates locomotor activity. Brain Res. *564*, 159–163.

62. Darmohray, D.M., Jacobs, J.R., Marques, H.G., and Carey, M.R. (2019). Spatial and temporal locomotor learning in mouse cerebellum. Neuron *102*, 217–231.e4.

63. Cabaj, A.M., Majczynski, H., Couto, E., Gardiner, P.F., Stecina, K., Slawinska, U., and Jordan, L.M. (2017). Serotonin controls initiation of locomotion and afferent modulation of coordination via 5-HT7 receptors in adult rats. J. Physiol. *595*, 301–320.

64. Stujenske, J.M., Spellman, T., and Gordon, J.A. (2015). Modeling the spatiotemporal dynamics of light and heat propagation for in vivo optogenetics. Cell Rep. *12*, 525–534.

65. Musienko, P.E., Zelenin, P.V., Lyalka, V.F., Gerasimenko, Y.P., Orlovsky, G.N., and Deliagina, T.G. (2012). Spinal and supraspinal control of the direction of stepping during locomotion. J. Neurosci. *32*, 17442–17453.

66. Karayannidou, A., Zelenin, P.V., Orlovsky, G.N., Sirota, M.G., Beloozerova, I.N., and Deliagina, T.G. (2009). Maintenance of lateral stability during standing and walking in the cat. J. Neurophysiol. *101*, 8–19.

67. Ghosh, K.K., Burns, L.D., Cocker, E.D., Nimmerjahn, A., Ziv, Y., Gamal, A.E., and Schnitzer, M.J. (2011). Miniaturized integration of a fluorescence microscope. Nat. Methods *8*, 871–878.

68. Dougherty, K.J., Zagoraiou, L., Satoh, D., Rozani, I., Doobar, S., Arber, S., Jessell, T.M., and Kiehn, O. (2013). Locomotor rhythm generation linked to the output of spinal shox2 excitatory interneurons. Neuron *80*, 920–933.

69. Kimura, Y., Okamura, Y., and Higashijima, S. (2006). alx, a zebrafish homolog of Chx10, marks ipsilateral descending excitatory interneurons that participate in the regulation of spinal locomotor circuits. J. Neurosci. *26*, 5684–5697.

70. Wu, J., Capelli, P., Bouvier, J., Goulding, M., Arber, S., and Fortin, G. (2017). A V0 core neuronal circuit for inspiration. Nat. Commun. *8*, 544.

71. Caggiano, V., Sur, M., and Bizzi, E. (2014). Rostro-caudal inhibition of hindlimb movements in the spinal cord of mice. PLoS ONE *9*, e100865.

72. Zingg, B., Chou, X.L., Zhang, Z.G., Mesik, L., Liang, F., Tao, H.W., and Zhang, L.I. (2017). AAV-mediated anterograde transsynaptic tagging: mapping corticocollicular input-defined neural pathways for defense behaviors. Neuron *93*, 33–47.

73. Mattis, J., Tye, K.M., Ferenczi, E.A., Ramakrishnan, C., O'Shea, D.J., Prakash, R., Gunaydin, L.A., Hyun, M., Fenno, L.E., Gradinaru, V., et al. (2011). Principles for applying optogenetic tools derived from direct comparative analysis of microbial opsins. Nat. Methods *9*, 159–172.

74. Harrison, M., O'Brien, A., Adams, L., Cowin, G., Ruitenberg, M.J., Sengul, G., and Watson, C. (2013). Vertebral landmarks for the identification of spinal cord segments in the mouse. Neuroimage *68*, 22–29.

75. Ueda, H.R., Ertürk, A., Chung, K., Gradinaru, V., Chédotal, A., Tomancak, P., and Keller, P.J. (2020). Tissue clearing and its applications in neuroscience. Nat. Rev. Neurosci. *21*, 61–79.

76. Franklin, K.B., and Paxinos, G. (2007). The Mouse Brain in Stereotaxic Coordinates, Third Edition (Elsevier).

77. Pearson, K.G., Acharya, H., and Fouad, K. (2005). A new electrode configuration for recording electromyographic activity in behaving mice. J. Neurosci. Methods *148*, 36–42.

78. Mathis, A., Mamidanna, P., Cury, K.M., Abe, T., Murthy, V.N., Mathis, M.W., and Bethge, M. (2018). DeepLabCut: markerless pose estimation of user-defined body parts with deep learning. Nat. Neurosci. *21*, 1281–1289.

Please cite this article in press as: Usseglio et al., Control of Orienting Movements and Locomotion by Projection-Defined Subsets of Brainstem V2a Neurons, Current Biology (2020), https://doi.org/10.1016/j.cub.2020.09.014

STAR★METHODS

KEY RESOURCES TABLE

REAGENT or RESOURCE	SOURCE	IDENTIFIER
Antibodies		
Goat anti-Choline Acetyltransferase (ChAT)	Merck Millipore	Cat #: AB144P; RRID: AB_2079751
Chicken anti-Green Fluorescent Protein (GFP) Antibody	Aves Labs	Cat #: 1020; RRID: AB_10000240
Rabbit anti-Red Fluorescent Protein (RFP)	Rockland	Cat #: 600-401-379; RRID: AB_2209751
Sheep anti-Tyrosine Hydroxylase (TH)	Merck Millipore	Cat #: AB1542; RRID: AB_90755
Bacterial and Virus Strains		
AAV8-hSyn-FLEX-TVA-p2a-eGFP-2a-oG	SALK GT3	RRID: Addgene_85225
HSV1-hEF1a-LS1L-TVA950-T2A-rabiesOG-IRES-mCherry	Rachael Neve	Rachael Neve, Massachusetts General Hospital
HSV1-hEF1a-LS1L-hChR2(H134R)-p2A-EYFP	Rachael Neve	Rachael Neve, Massachusetts General Hospital
EnvA-ΔG-Rabies-mCherry	SALK GT3	RRID: Addgene_32636
EnvA-ΔG-Rabies-GFP	SALK GT3	RRID: Addgene_32635
AAV9-Ef1a-DIO-hChR2(E123T/T159C)-EYFP	Addgene	RRID: Addgene_35509
AAV5-FLEX-taCasp3-TEVp	UNC	RRID: Addgene_45580
AAV8.2-hEF1a-DIO-hM4Di-mCherry-WPRE	Rachael Neve	Rachael Neve, Massachusetts General Hospital
AAVretro-EF1a-doublefloxed-hChR2(H134R)-EYFP-WPRE-HGHpA	Addgene	RRID: Addgene_20298
Chemicals, Peptides, and Recombinant Proteins		
Clozapine N-oxide (CNO)	Enzo Life Sciences	Cat #: BML-NS105-0005
Cholera Toxin B (CTB) – AF647 conjugate	ThermoFisher Scientific	Cat #: C-34778
NeuroTrace 640/660 Deep-Red	ThermoFisher Scientific	Cat #: N21483
NeuroTrace 435/445 blue	ThermoFisher Scientific	Cat #: N21479
Fluoro-Max blue beads	ThermoFisher Scientific	Cat #: B500
Prolong Diamond Antifade Montant	ThermoFisher Scientific	Cat #: P36970
ibidi Mounting Medium	ibidi	Cat #: 50001
Deposited Data		
Original datasets on Mendeley Data	This paper	http://doi.org/10.17632/54x8rjppfz.1
Experimental Models: Organisms/Strains		
Mouse: Chx10-Cre	S. Crone, K. Sharma, L. Zagoraiou, and T.M. Jessell	[34, 38, 39]
Software and Algorithms		
MATLAB R2018a	Mathworks	https://www.mathworks.com/products/matlab.html; RRID: SCR_001622
DeelLabCut	Mathis Lab	http://www.mousemotorlab.org/deeplabcut
ImageJ	https://imagej.net/	RRID: SCR_003070
ZEN Lite	Zeiss	https://www.zeiss.fr/microscopie/produits/microscope-software/zen-lite/zen-2-lite-download.html; RRID: SCR_013672
Leica LASX	Leica	https://www.leica-microsystems.com/products/microscope-software/p/leica-las-x-ls/; RRID: SCR_013673
LabScribe NI	iWorxs	https://www.iworx.com/products/biomedical-engineering/labscribeni/
2nd LOOK	IO Industries	http://ioindustries.com/2ndlook.html
Kdenlive video editor	Kdenlive	https://kdenlive.org/fr/

Please cite this article in press as: Usseglio et al., Control of Orienting Movements and Locomotion by Projection-Defined Subsets of Brainstem V2a Neurons, Current Biology (2020), https://doi.org/10.1016/j.cub.2020.09.014

RESOURCE AVAILABILITY

Lead Contact

Further information and requests for resources and reagents should be directed to and will be fulfilled by the Lead Contact, Julien Bouvier (julien.bouvier@cnrs.fr).

Materials Availability

This study did not generate new unique reagents.

Data and Code Availability

Original data have been deposited to Mendeley Data (http://dx.doi.org/10.17632/54x8rjppfz.1). This study did not generate any computer code.

EXPERIMENTAL MODEL AND SUBJECT DETAILS

Mice

The *Chx10-Cre* was kindly provided by S. Crone, K. Sharma, L. Zagoraiou, and T.M. Jessell [34, 38, 39]. C57BL6 wilt-type mice were obtained by Janvier Labs (Le Genest-Saint-Isle, France). Animals were group-housed with free access to food and water in controlled temperature conditions and exposed to a conventional 12-h light/dark cycle. Experiments were performed on animals of either sex, aged 2 to 3 months at the time of first injection. All procedures were approved by the French Ethical Committee (authorization 2020-022410231878) and conducted in accordance with EU Directive 2010/63/EU. All efforts were made to reduce animal suffering and minimize the number of animals.

Viruses used

For Cre-dependent expression of ChR2 in the Gi we injected unilaterally 100 to 200 nL of an AAV9-Ef1a-DIO-hChR2(E123T/T159C)-eYFP (addgene #35509, titer 3.2×10^{12} vp/mL [73]). For cellular ablation of V2a Gi neurons we used 400 nL of a AAV5-FLEX-taCasp3-TEVp (titer 4.6×10^{12} vp/mL) obtained from UNC (addgene plasmid #45580 [43]). For reversible silencing of V2a Gi neurons we used 400 nL of a AAV8.2-hEF1a-DIO-hM4Di-mCherry-WPRE (titer 2.25×10^{13}) obtained from Dr. Rachael Neve (Gene Delivery Technology Core, Massachusetts General Hospital, USA). For transsynaptic labeling of inputs onto V2a Gi neurons, we used 500 nL of an AAV8-hSyn-FLEX-TVA-p2a-eGFP-2a-oG (titer: 2.8×10^{12} vp/mL) obtained by the GT3 core (Salk Institute). For retrograde labeling of spinally-projecting V2a neurons we used 500nL per injection spot of HSV1-hEF1a-LS1L-TVA950-T2A-rabiesOG-IRES-mCherry and HSV1-hEF1a-LS1L-hChR2(H134R)-p2A-eYFP obtained from Dr. Rachael Neve (Gene Delivery Technology Core, Massachusetts General Hospital, USA). Rabies viruses used were EnvA-ΔG-rabies-mCherry (titer: 3.12×10^{8} vp/mL) and EnvA-ΔG-rabies-GFP (titer: 2.26×10^{8} vp/mL) both obtained by the GT3 core (Salk Institute, USA). For optogenetic manipulations of spinally-projecting V2a neurons we used 500 nL per injection spot of AAVretro-EF1a-doublefloxed-hChR2(H134R)-eYFP-WPRE-HGHpA (Karl Deisseroth, Addgene plasmid # 20298; http://n2t.net/addgene:20298; RRID: Addgene_20298; titer 1.0×10^{13} vp/mL).

METHOD DETAILS

Surgical procedures for injections and implants in the brainstem

Animals were anesthetized with isoflurane throughout the surgery (4% at 1 L/min for induction, and 2%–3% at 0.3 L/min for maintenance). Buprenorphine (0,025 mg/kg) was administered subcutaneously for analgesia before the surgery. The temperature of the mice was maintained at 36°C with a feedback-controlled heating pad. Anesthetized animals were placed on a stereotaxic frame (Kopf) and the skull was exposed. Viral vectors were delivered using a pulled glass pipette connected to a syringe pump (Legato 130, KD Scientific, customized by Phymep, France). The infusion flow was set to 100 nL/min. Coordinates (in mm) used to target V2a Gi neurons were: −6.0 from bregma, 0.8 lateral, and 4.5 from the dorsal brain surface. After the injection, the pipette was held in place for 5 min before being slowly retracted. For optogenetic activations, a 200 μm core 0.39 NA optic fiber (Thorlabs) connected to a 1.25 mm diameter ferrule (Thorlabs) was implanted ∼500 μm above the injection site (Figure 2A). This operation was performed during the same surgery as the viral injection when both were targeted to the brainstem. For activating spinally-projecting V2a neurons, the spinal injection was performed first (see below) and the optic fiber was implanted 5 to 7 days later. Dental cement (Tetric Evoflow) was used to secure the implanted ferrules. Animals were followed daily after the surgery.

Surgical procedures for injections in the spinal cord

Animals were anesthetized as described above and spinal injections were performed as previously done [34]. A two cm incision of the skin was performed dorsally on anesthetized animals and the exposed spinal column was fixed with two holders on the left and right sides to a stereotaxic frame to minimize movements. Vertebral spinous processes were used as landmarks to target specific segments [74]. A small incision of the ligamentum Flavum allowed access to the spinal cord. A pulled glass pipette connected to

Please cite this article in press as: Usseglio et al., Control of Orienting Movements and Locomotion by Projection-Defined Subsets of Brainstem V2a Neurons, Current Biology (2020), https://doi.org/10.1016/j.cub.2020.09.014

a motorized syringe pump injector (Legato 130, KD Scientific, customized by Phymep, France) was positioned into the ventromedial area of the L2 (between the 11th and 12th vertebral body) or C2 (between the 1st and 2nd vertebral body) spinal segment using the following coordinates: 400 mm laterally from the dorsal artery and 500 to 850 mm (L2 injections) or 800 to 1200 μm (C2 injections) depth from the dorsal surface. This lateral positioning ensures that the injection pipette does not pass through the lateral funiculus where descending axons of RS neurons travel. A total volume of 500 nL of virus was injected at 100 nL/min in 2 distinct spots separated rostrocaudally by 600 to 800 μm. For CTB injections, we used 500 nL of CTB-AF647 conjugate (Thermofisher Scientific, Cat # C-34778) diluted at 0.5% in sterile saline. Dual HSVs injections (Figures 4J and S4) were done bilaterally to increase the number of labeled cells for quantifications but AAVretro injections (Figures 5, 6, and S6) were done unilaterally. Dual injections of HSVs in both the L2 and C2 spinal segments were performed successively, starting from L2, during the same surgical procedure. For controls, two consecutive HSV injections were performed at L2, either during the same day or at one day apart (Figure S4). After each injection, the pipette was held in place for 5 min before being slowly retracted. The skin was sutured, and animals were followed daily after the surgery. All animals recovered without motor impairments.

Histology

Adult mice were anesthetized with Euthasol Vet (140 mg/kg) and perfused with 4% paraformaldehyde (PFA) in 1X Phosphate Buffered Saline (PBS). Brains and spinal cord were dissected out and fixed overnight in 4% PFA at 4°C. After fixation, tissues were rinsed in 1X PBS. Brain and spinal cord were cryoprotected overnight at 4°C, respectively in 16% and 20% sucrose in PBS. Tissues were rapidly cryoembedded in OCT mounting medium and sectioned at 30 μm using a cryostat. Sections were blocked in a solution of 1X Tris Buffered Saline (TBS), 5% normal donkey serum and 0.5% Triton X-100. The primary antibodies, carried out 24 to 48 h at 4°C, were: goat anti-ChAt (1:500, ref: AB144P, Merck Millipore), chicken anti-GFP (1:500, ref: 1020, Aves Labs), rabbit anti-RFP (1:500, ref: 600-401-379, Rockland) and sheep anti-TH (1:500, ref: AB1542, Merck Millipore). Primary antibodies were detected after 2 h of incubation at room temperature with appropriate secondary antibodies coupled to Alexa Fluor 488, 647, Cy-3 or Cy-5 (1:500, Jackson ImmunoResearch). Sections were counterstained with a fluorescent Nissl stain (NeuroTrace 435/445 blue, ref: N21479, 1:200 or NeuroTrace 640/660 deep-red, ref: N21483, 1:1000, Thermo Fisher Scientific) and mounted in Prolong Diamond Antifade Montant (P36970, Thermo Fisher Scientific) or ibidi Mounting Medium (50001, Ibidi). For counting neurons in the entire brain in transneuronal labeling experiments, all sections were scanned on a Zeiss Axioscan Z1 Digital Slide Scanner (histology platform of the ICM, Paris, France). For all other purposes, sections were acquired with a Leica TCS SP8 confocal microscope (imaging platform of the NeuroPSI Institute, Gif-sur-Yvette, France) with 10x, 25x and 40x objectives. For illustrating a representative spinal cord injection (Figure 4F), whole lumbar spinal cords were cleared using CUBIC-R+ [75] and endogenous CTB fluorescence imaged on a light-sheet microscope (UltraMicroscope II, 4x objective, Miltenyi Biotec).

Delineation of brainstem structures and cellular counts

Brainstem areas were delineated by systematically performing a Nissl stain on experimental sections. The relative distance to Bregma was established by comparing the Nissl stain with that of the Mouse Brain atlas [76]. To examine the distribution of labeled neurons within the rostrocaudal axis of the RF, we considered four major subdivisions, similarly to a previous investigation [34] on the basis of the following criteria (see schematics in Figures 1C and 4G): the most caudal levels (encompassing the MdV) from the rostral edge of the pyramidal decussation caudally, to the opening of the 4th ventricle (obex) rostrally (from approximately −8.0 to −7.2 from Bregma); the caudal extent of the Gigantocellular reticular (Gi) nucleus (encompassing also its ventral part GiV) between the obex caudally and the caudal edge of the facial motor nucleus (7N) rostrally (approximately −6.5 from Bregma); the rostral extent of the Gi nucleus (encompassing its alpha part GiA and the IRt) from the caudal edge of the 7N caudally, to the caudal edge of the superior olivary complex (SOC) rostrally (approximately −5.5 from Bregma); the ponto-medularry junction (encompassing the PnC and the IRt) from caudal edge of the SOC to the motor trigeminal nucleus rostrally (approximately - 5.0 from Bregma). All neurons were counted on 30 μm-thick cryosections. For counting starter cells (Figures 1A–1E and S5) and HSV-labeled neurons (Figures 4 and S4), sections were scanned with a confocal microscope (Leica SP8) using a 25x objective. Counts were done manually with the help of the cell-counter tool in LASX (Leica), in non-adjacent sections. The number of cells per section were averaged per animal, and a grand-mean ± standard error of the mean (SEM) was calculated across animals to produce cells per section bar graphs. At each of the four rostrocaudal subdivision, labeled neurons were allocated into specific subnuclei (e.g., Gi, GiV, GiA, LPGi, IRt, PnC) by overlaying the histological section to the corresponding atlas slide. Pie graphs illustrate the fraction of labeled neurons located in each subnuclei (pooled from all animals) over the total number of labeled contained in the corresponding rostrocaudal subdivision. For counting rabies-labeled neurons, images were obtained from an automated epifluorescence microscope (Zeiss Axioscan Z1 Digital Slide Scanner). For illustrating the percentage of rabies-labeled neurons in each brain area (Figures 1J, S5E, and S5J) neurons in each area were counted using ZEN-Lite (Zeiss) and pooled across all sections for one animal, and expressed as the fraction of the total number of rabies-positive neurons detected automatically by threshold throughout the brain in that same animal. A grand-mean ± SEM was calculated across animals to produce bar graphs. For calculating the fractions of fluorescent anterograde projections in different structures (Figure 4E), maximum z stack projections were made and thresholded. Regions of interests were manually drawn in ImageJ and the densities of fluorescent pixels were measured for 4-5 sections per animal using the Measure plugin. These values were averaged across all sections from all animals and expressed in bar graphs ± SEM.

Please cite this article in press as: Usseglio et al., Control of Orienting Movements and Locomotion by Projection-Defined Subsets of Brainstem V2a Neurons, Current Biology (2020), https://doi.org/10.1016/j.cub.2020.09.014

Behavioral experiments

Optogenetic activations

Behavioral experiments started 15 to 21 days after the viral injection. Implanted animals were connected to a laser source (473 nm DPSS system, LaserGlow Technologies, Toronto, Canada) through a mating sleeve (Thorlabs). In all conditions except EMG recordings, light was delivered in trains of pulses of 15 ms at 40 Hz frequency for a duration of 500 ms. For EMG recordings we also used single pulses of 5 ms duration. We used the minimal laser power sufficient to evoke a response, which was measured to be between 5-12 mW at the fiber tip using a power meter (PM100USB with S120C silicon power head, Thorlabs) to restrict photo-activations unilaterally [64], prevent heat, and exclude an unintentional silencing by over-activation [34].

Behavioral setting and video recordings

For analyzing changes in head movements, trajectory orientation and locomotor speed, animals were placed in a custom open field box (opaque PVC, 60 × 70 cm) without prior habituation and filmed from above at 50 images/sec using a CMOS camera (Jai GO-5000-USB). For analyzing limb movements during optogenetic activations, animals were placed in a custom transparent open-field (40 × 40 cm) and filmed from below at 100 images/sec (Jai GO-2400-USB). For optogenetic activations, open-field recording sessions lasted for a maximum of 30 min per animal. For silencing and ablation experiments, several 3-min videos were recorded per animal. For analyzing snout motion, animals were head-fixed for a maximum of 10 min, and filmed from above at 400 images/sec (Jai GO-2400–USB). Images were streamed to disk on a computer using 2nd Look (IO Industries). Timings of photo-activations were recorded using the TTL output of the laser connected to a National Instruments acquisition card (USB-6211) and the LabScribe NI software (iWorxs). Both recordings were synchronized using hardware trigger. Photo-activations were delivered manually using the NI MAX tool with a minimal interval of 30 s between two consecutive activations. Throughout the manuscript, one trial correspond to one photo-activation. Extracts of videos presented in the supplemental material were edited using Kdenlive (https://kdenlive.org/).

CNO administration

Four weeks following the injection of the hM4Di virus, animals were anesthetized and a surgery was performed as detailed earlier for intracranial viral injection. CNO (Enzo Life science, cat #: BML-NS105-0005) was diluted at 1 mM in freshly made and filtered artificial cerebrospinal fluid (aCSF) of composition (in mM): 126 NaCl; 3 KCl; 1.25 NaH_2PO_4; 2 $MgSO_4$; 26 $NaHCO_3$; 2 CaCl2; 11 D-Glucose. Fluorescent beads (Fluoro-Max blue beads, 0.5 μm, ThermoFischer Scientific, Cat#: B500) were added at a dilution of 1:4000 for subsequent histological validation. A total of 500 nL of CNO/fluorescent beads solution was delivered at the same coordinates used for the hM4Di virus (left side: 4 animals, right side: 1 animal). The pipette was immediately withdrawn after the injection, the skin incision closed rapidly with surgical glue (Vetbond, 3M Cat#: 1469SB) and animals immediately removed from the anesthesia mask. They were kept on an isothermal heating pad (Agnthos, Sweden) for a maximum of 10 min before being placed in the open-field to be filmed from above during 3 min. Since animals had only partially recovered from anesthesia, occasional motivation to move was given by a brief air puff or by the experimenter's hand. Animals were placed back on the heat pad for 2 min, before being filmed again in the open field for 3 min. The 2 videos started within the 15 min that follow the pipette withdrawal are used to produce the "CNO < 15 min" data (Figure 3O). Two or 3 more videos are recorded between 16 and 30 min following pipette withdrawal and used to produce the "CNO > 15 min" data. For controls, similar CNO injections were done on animals that did not receive the hM4Di virus.

Electromyographic Recordings

Electrodes were made of Teflon-insulated silver wire with an outside diameter of 0.14 mm (A-M systems, #793200), inspired by previous work [77]. For each animal, 2 pairs of electrodes were prepared as follows. For each electrode pair, two pieces of wire were lightly twisted together and a knot was placed about 2 cm of one end. A few millimeters from the knot, the Teflon insulation was removed over ~1 mm from each wire so that the two bared regions were separated by about 2 mm. The ends of two wires were glued to a miniature dissecting pin. The opposite ends of the wires were soldered to a miniature connector (Antelec). To implant electrodes in the splenius muscle, animals were anaesthetized using isoflurane and placed in a stereotaxic frame as detailed above. A small incision of the skin was performed dorsally to expose the muscles. The dissecting pin attached to the end of each pair of electrodes was used to draw the twisted pair of wires through the splenius muscle until the knot proximal to the bared regions was firmly against the muscle. The distal end of the electrode exiting the muscle was knotted. The needle was removed by cutting the electrode wires about 0.5 mm distal to this knot. The miniaturized connector was cemented on the skull, caudally to the existing optic fiber. The skin was sutured, and animals were followed daily after the surgery. Between 2 to 3 days following the surgery, implanted animals were connected to an AC amplifier (BMA-400, CWE) and signals were filtered (high-pass: 100 Hz, low-pass: 10 KHz) and collected at 10.000 samples/sec using a National Acquisition card (USB 6211) and the LabScribe NI software (iWorxs). Animals were placed in the open-field and optogenetic activations were delivered manually using the NI MAX tool. A TTL signal from the laser was connected to the same acquisition board for registering the timing of optogenetic activations.

QUANTIFICATION AND STATISTICAL ANALYSIS

Pose estimation using DeepLabCut and quantifications of body and head movements

To compute changes in body orientation, head rotation and locomotor speed, we labeled manually 4 points of interest (POIs) from 3204 frames taken across 80 top-view videos using DeepLabCut version 2.1.5.2 [78]: the head (H), the left and right ears (E_L, E_r) and

the base of the tail (T, see Figure S2A). We then used 95% of the labeled frames to train the network using a ResNet-101-based neural network with default parameters for 1 training iteration. We validated with 3 shuffles, and found that the test error was: 3,84 pixels, train: 3,21 pixels (image size was 2384 by 2048). We then used a p-cutoff of 0,5 to condition the X,Y coordinates for future analyses. This network was then used to analyze all other videos taken with same experimental settings.

Custom scripts were written in MATLAB (Mathworks) and used for computation. The orientation of the animal is defined as the angle α between the vector from T to the median point of E_L and E_R (E_M) and the origin axis $\overrightarrow{x}$ (Figure S2B).

$$\frac{\overrightarrow{TE_M}}{\left\|\overrightarrow{TE_M}\right\|} = \begin{pmatrix} X_1 \\ Y_1 \end{pmatrix}$$

$$\begin{pmatrix} X_1 \\ Y_1 \end{pmatrix} = \begin{pmatrix} \cos(\alpha) & -\sin(\alpha) \\ \sin(\alpha) & \cos(\alpha) \end{pmatrix} * \begin{pmatrix} 1 \\ 0 \end{pmatrix}$$

$$\alpha mod 360 = sign(Y_1) * \cos^{-1}(X_1)$$

The head rotation is defined by the angle β between the vector from T to E_M and the vector from E_L to E_R. A bias of 90° is introduced to set the zero when the 2 vectors are orthogonal, resulting in a positive angle when the head turns to the left and a negative angle when the head turns to the right (Figure S2C).

$$\frac{\overrightarrow{E_L E_R}}{\left\|\overrightarrow{E_L E_R}\right\|} = \begin{pmatrix} X_0 \\ Y_0 \end{pmatrix}$$

$$\begin{pmatrix} X_1 \\ Y_1 \end{pmatrix} = \begin{pmatrix} \cos(\beta) & -\sin(\beta) \\ \sin(\beta) & \cos(\beta) \end{pmatrix} * \begin{pmatrix} X_0 \\ Y_0 \end{pmatrix}$$

$$\beta mod 360 = sign\left(\frac{Y_1 - (X_0 X_1 + Y_0 Y_1) Y_0}{X_0}\right) * \cos^{-1}(X_0 X_1 + Y_0 Y_1) - 90$$

The barycenter (G) of the 4 POIs was computed to generate the locomotor trajectory of each mouse and its position derived to obtained the instantaneous speed (s) of the animal across the recording (Figure S2D).

$$\overrightarrow{s} = \frac{\partial \overrightarrow{u}}{\partial t}$$

With $\overrightarrow{u}$ being the displacement of G

$$\overrightarrow{u} = \overrightarrow{x} + \overrightarrow{y} \text{ and } \begin{cases} \overrightarrow{s_x} = \dfrac{\partial \overrightarrow{x}}{\partial t}, \overrightarrow{x} \text{ being the displacement of G along the x axis} \\ \overrightarrow{s_y} = \dfrac{\partial \overrightarrow{y}}{\partial t}, \overrightarrow{y} \text{ being the displacement of G along the y axis} \end{cases}$$

$$\overrightarrow{s} = \overrightarrow{s_x} + \overrightarrow{s_y} \text{ and} \overrightarrow{s_x} \perp \overrightarrow{s_y}$$

$$s = \sqrt{s_x^2 + s_y^2}$$

For optogenetic activations, trials were sorted as during locomotion when the animal's instantaneous speed was above 10 cm/s and during stationary when it was under 7.5 cm/s during 250 consecutive ms prior to light onset. Indeed, when animals were between these 2 speed values, their behavior was difficult to score (some steps interleaved with immobility) and corresponding trials were therefore not included. For each mouse, trials falling into either category (locomoting or stationary) were merged into matrices and each variable computed (var: α, β, speed):

$$A_{var} = \begin{pmatrix} a_{1,1} & \cdots & a_{1,j} \\ \vdots & \ddots & \vdots \\ a_{i,1} & \cdots & a_{i,j} \end{pmatrix}$$

with i the number of trials and j the number of frames per trial.

In the case of angles (ex: α, β), we normalized, at each trial, the changes induced by light stimulation to the average angle during 0,5 s before light onset.

Please cite this article in press as: Usseglio et al., Control of Orienting Movements and Locomotion by Projection-Defined Subsets of Brainstem V2a Neurons, Current Biology (2020), https://doi.org/10.1016/j.cub.2020.09.014

Finally for each type of injection (Gi, C2, L2) and behavioral condition (stationary or locomoting), the mean response of each animal was computed across all trials (the same number of trials per animal, at least 3 trials) and expressed ± standard error (SEM). A grand-mean ± SEM across animals is also illustrated in figures (colored curves).

Calculations of limb velocity

To produce color-plots histograms, we attempted to label the 4 paws using DeepLabCut. However, this led to significant number of errors and inversions between paws. All errors were then manually corrected on 9 videos from 3 mice. Points were then filtered (maximum speed and group cutoff followed by linear interpolation) and the instantaneous speed of each limb speed was then computed, and a color matrix produced using MATLAB.

Statistical analysis for optogenetic experiments

To perform statistical tests for body orientation, we calculated, for each trial, the peak change in orientation of the mouse during photo-activations as well as the orientation 0.5 s after light offset (black arrowhead in graphs). For the head rotation, we calculated the maximum angle variation to baseline during photo-activations. Both the body orientation and head rotation angles of all trials (numbers are given in figure legends) from all mice within each category (i.e., Gi, L2 or C2 injection and stationary or locomoting) were statistically compared to the same measurements obtained from all trials from 4 injected and implanted wild-type mice (stationary: 44 trials from 4 mice, 11 trials each; locomotion: 48 trials from 4 mice, 12 trials each), using unpaired t tests. For evaluating the effect of photo-activations on locomotor speed we took into account the spontaneous gradual deceleration that occurs independently of activating V2a neurons, as seen in mock photo-activation trials in control mice (Figure S2K). This likely owes to the episodic nature of locomotion in this specie and our intentional delivery of photo-activations when animals just engaged in a vigorous locomotor bout which is bound to be short due to the limited size of the open field. We therefore computed, for each trial, the mean locomotor speed during light stimulations as well as the first deceleration coefficient of the first monotonic part of the curve during the light-stimulation as the best fitted linear regression. Both the mean speed and the slope coefficients of all trials of all mice within a given category were statistically compared to those obtained from control mice. For snout motion recordings, the mean position of the nose snout during the 500 ms photo-activations was computed for each trial, and statistically compared to the mean position during the preceding 500 ms.

Statistical analysis for ablation and silencing experiments

We computed, for each video of each mice, i) the instantaneous angular speed of the animal as the first derivative of the body orientation during locomotion (i.e., instantaneous speed > 10 cm/s) and ii) the average head orientation during the entire video recording. These values were statistically compared between appropriate groups (e.g., before and after CNO) using unpaired t tests.

Statistical analysis for electromyographic recordings

EMG recordings were exported to Clampfit (Molecular Devices) and responses to photo-activations were detected manually as events with a pointed peak (either negative of positive), with an amplitude larger than 5 times the mean baseline before the light pulse and occurring within 25 ms following light onset. The latency was defined as the interval between light onset and the time point when the EGM signal reaches the above detection threshold. Data were collected for ~15 trials per animal and a grand-mean ± SEM across all trials was computed to produce bar graphs illustrated in Figure 7. Differences in latency between the ipsilateral and contralateral sides were evaluated by unpaired t tests across all trials.